Unmanned Systems, Vol. 14, No. 2 (2026) 415–439

DOI: 10.1142/S2301385026500093

UNMANNED SYSTEMS
https://www.worldscientific.com/worldscinet/us

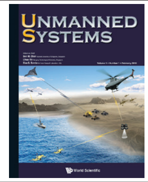

Enhanced Approaches of Precision Thrust Vector Control for Aerial Vehicles: Comprehensive Modeling and Validation

Mohamed M. Ahmed [*,‡], Gamal M. ElBayoumi [*,§], Ahmed E. Elbanna [†,¶]

[*] *Aerospace Department, Faculty of Engineering, Cairo University, Cairo, Egypt*

[†] *College Arab Academy for Science, Technology & Maritime Transport, Cairo, Egypt*

The Thrust vector control (TVC) is a method for controlling the angular velocity and attitude of aerial vehicles (AV) by manipulating the thrust direction of propulsion. This technology enhances maneuverability and allows for dynamic aerobatics at low speeds and near-zero airspeeds without stalling at high angles of attack (AOA). As the aerodynamic control surfaces are ineffective for vehicles operating outside the atmosphere, TVC is a suitable technique for these applications. To design a control system for AVs utilizing TVC, an accurate mathematical model is essential to simulate flight parameters and optimize the control gains. This work presents a complete six degrees-of-freedom (6-DOF) high-fidelity simulation model of a thrust vector control aerial vehicle (TVC-AV). The nonlinear model is developed by dividing the mathematical representation into five submodules, including the geometrical model, the actuation model that was experimentally identified, and an aerodynamic model that was validated through semi-empirical techniques, computational fluid dynamics (CFD), and wind-tunnel experiments; in addition, the propulsion model's characteristics are identified through experimentation, and the atmospheric model is based on International Standard Atmosphere (ISA) values. The integrated model was implemented in MATLAB® (Simulink) that provides a foundation for designing effective flight controllers and guidance systems.

Keywords: Thrust vector control; unmanned aerial vehicle; modeling; aerodynamics; flight mechanics.

1. Introduction

The thrust vector control (TVC) adjusts the thrust direction of vehicles to enhance trajectory precision and agility, allowing aerial vehicles (AVs) to make precise flight path modifications. TVC increases maneuverability, enabling near-zero airspeed at steep angles of attack without stalling and facilitating dynamic aerobatics at lower speeds [1].

The TVC principles involve shifting the center of pressure (CP) by altering the thrust vector direction, which stabilizes the flight path [2]. By directing thrust, moments act on the vehicle's mass, causing rotation and trajectory alteration. TVC also counteracts external forces, such as crosswinds and turbulence, by redirecting thrust [3].

In many AVs, thrust vectoring is achieved by gimbaling the entire engine or deflecting only the engine nozzle using electric actuators or hydraulic cylinders [4]. The nozzle is typically attached via a ball-joint or flexible, which requires more torque and a robust actuation system [5].

For the case study vehicle, the ball-joint method is used for pitch and yaw control, while four canard surfaces assist in roll control due to the single-engine setup. Designing an accurate control system for TVC necessitates a precise mathematical model to simulate the UAV's dynamic behavior and response to various excitations [6, 7]. This modeling aids in understanding the parameters impacts on performance, simulating flight conditions, and assisting control engineers in tuning parameters, thus saving time and resources in preliminary flight tests [8].

A precise mathematical description of UAVs is essential for effective model-based control techniques. UAV modeling is categorized into physics-based modeling and system identification [9]. While system identification is generally more accurate, it is also time-consuming and costly due to

Received 19 September 2024; Accepted 16 January 2025; Published 18 March 2025. This paper was recommended for publication in its revised form by editorial board member, Jianan Wang.

Email Addresses: [‡] *eng.m.mahran1992@gmail.com*, [§] *gelbayoumi@cu.edu.eg*, [¶] *ahmedelbanna80@adj.aast.edu*

[‡] Corresponding author.

the need for flight tests. In contrast, physics-based modeling is faster and more economical, often requiring only one flight test for tuning [10].

The UAV dynamic model consists of several sub-models: geometric mass inertia model, atmospheric, actuation, propulsion, and aerodynamic models. These can be estimated through various methods, including theoretical, computational, semi-empirical, numerical, and experimental approaches. For example, the UAV inertia model may be estimated using advanced CAD tools or experimentally for smaller platforms. The atmospheric model is typically described theoretically, while the aerodynamic model is based on data from the USAF Stability and Control Digital DATCOM program, computational fluid dynamics simulation (CFD), or experimentally approach wing wind tunnel.

For the aerodynamic model, to validate the DATCOM results, the CFD approach can be employed using ANSYS software, known for its high accuracy (up to 95%) but requiring significant processing time and hardware resources. Therefore, DATCOM can be utilized during preliminary design stages with 75% accuracy, while ANSYS will validate results in the final stage. Although ANSYS can replace wind-tunnel experiments, this paper presents various types of experiments to ensure comprehensive validation of the aerodynamic model.

In the evolving landscape of thrust vector control (TVC) for aerial vehicles, researchers have made substantial strides, yet critical gaps remain. Each study contributes valuable insights while also revealing limitations that highlight the need for further investigation. The following paragraphs present some of these studies, outlining their contributions and drawbacks. The contributions of this paper, however, offer potential solutions to some of these identified drawbacks.

Starting with Kapeel [11], who developed a nonlinear 6-DOF simulation model for a fixed-wing UAV, the work is commendable for its comprehensive methodology. However, it heavily relies on experimental data for mass-inertia modeling and does not adequately account for environmental variations, such as temperature and pressure that could impact flight dynamics. This raises concerns about the model's adaptability to different operational conditions.

Following this, Harris [12] explored the design of a Liquid Injection Thrust Vector Control (LITVC) system within modern jet propulsion technologies. While the study effectively discusses thrust vector control techniques, it primarily focuses on the high-performance propellants' immediate performance without delving into the long-term reliability of such systems under real-world conditions. The investigation could benefit from an exploration of how sustained high temperatures and multiphase flows affect thrust consistency over time.

Meanwhile, Nidal [13] approximated the aerodynamic model using DATCOM software, which adheres to NACA standards for wing airfoils. Although this approach provides a solid foundation, it is limited by the assumptions inherent in the DATCOM method, which may not fully capture the complexities of real-world aerodynamics. Furthermore, the lack of an experimental test with a different setup could lead to inaccuracies, particularly for UAVs operating in varying load conditions.

In a practical application, Ahmet [14] developed a new thrust sensor system tested at TÜBİTAK SAGE motor facilities. While the experimental results demonstrated reliability in thrust measurements, the study failed to address the implications of thrust misalignment due to nozzle wear over time. Understanding these long-term effects is crucial for ensuring consistent performance during prolonged operations.

Turning to Pedro [15], he introduced a nonlinear 6-DOF model employed for low-cost, small-scale motors. The architecture shows contribution but is built on assumptions of ideal operating conditions. The use of a linearized model for control and estimation may neglect the complexities of real flight scenarios, where disturbances and model uncertainties play significant roles in system performance.

Clinton [16] discussed the use of gimbaled thrust for future Nuclear Thermal Rocket missions, emphasizing its potential to reduce the burden on Reaction Control Systems (RCS). However, while the 6-DOF simulation model demonstrated effective control under varied parameters, it lacked a thorough investigation into how different mass moments of inertia and thrust imbalances might complicate control efforts, particularly during dynamic maneuvers.

Kargin [17] employed a semi-empirical approach to develop a dynamic model for a fixed-wing UAV using FORTRAN. While this approach offers a structured methodology, it may fall short in precision due to the generalization of aerodynamic characteristics, which can vary widely in actual flight.

In her comparative analysis, Laura [18] assessed multiple controllers, including PID, LQR, and LQG, for the TVC subsystem. While her results indicated the PID controller's superiority in managing disturbances, the study did not explore how these controllers might adapt to rapid changes in flight conditions, limiting the practical applicability of her conclusions.

Lastly, Mueller [19] and Leong [20] both designed UAV models using MATLAB® (Simulink) with different aerodynamic and propulsion frameworks. While these studies provide essential data, their reliance on specific software tools and simplifications raises concerns about the fidelity of the models in capturing complex flight dynamics.

In summary, while the existing literature presents a wealth of methodologies, contributions and results, it reveals significant limitations regarding environmental adaptability, long-term reliability, and practical implementation in varied conditions. These gaps underscore the motivation for our research, as we seek to advance the understanding and application of thrust vector control systems for aerial vehicles, giving a chance for more resilient and adaptable flight technologies.

The main contribution of this paper is the development of a comprehensive, validated nonlinear 6-DOF model for a thrust vector control aerial vehicle (TVC-AV), integrating advanced physical modeling techniques, high-accuracy sensors, and empirical validation through wind-tunnel experiments and computational fluid dynamics (CFD) analysis.

The model also incorporates elements of randomness or uncertainty in its parameters and system dynamics. This allows the model to better simulate real-world conditions where various factors, such as environmental disturbances or sensor noise, can affect the UAV's performance. Overcoming the drawbacks identified in the literature review, some procedures were employed to achieve this goal.

For instance, Kapeel [11] and Nidal [13] utilized less accurate inertia calculations and lack of experimental test; our use of higher-grade sensors enhances the precision of the inertia sub-model, ensuring a more reliable representation of UAV dynamics. Furthermore, the neglecting of the real-world parameter variation was compensated for in this work.

The actuator model developed through system identification techniques improves upon Harris's [12] methods, offering precise evaluation of motor dynamics while minimizing delays associated with microcontrollers. This advancement enhances the drawbacks noted in existing literature.

To estimate aerodynamic properties, we employ DATCOM in combination with MATLAB® (Simulink), which provides a more efficient and accurate alternative to the simplistic aerodynamic modeling methods found in Kargin [17]. The accuracy of these estimations is validated using ANSYS software and confirmed through experimental wind-tunnel measurements, thus filling gaps identified in Clinton's [16] work regarding empirical validation.

Our study also introduces cost-effective methods for conducting wind-tunnel experiments, addressing the time and resource constraints often faced in experimental setups. Also, the propulsion model is identified as a black box, utilizing pulse-width modulation (PWM) to ensure a robust validation process through multiple data sets. This approach strengthens the reliability of the propulsion sub-model, countering the limitations seen in Pedro's [15] study.

Overall, these methodologies enhance the accuracy, efficiency, and empirical support of our model, offering significant improvements over existing literature.

The structure of this paper is arranged as follows: Section 2 describes the mathematical model. Section 3 illustrates the modeling of the sub-models with comprehensive analysis. The development of the 6-DOF nonlinear model and its trim calculations are described in Sec. 4. Results of the open-loop simulation are analyzed in Sec. 5. Finally, the conclusion and future work are represented in Sec. 6.

2. UAV Mathematical Model

The UAV is considered a rigid body for the mathematical representation of the UAV model which consists of nonlinear differential equations that describe UAV motion in 3D or simulate UAV flight dynamics. First, for developing a nonlinear simulation model for the UAV, it's needed to develop the mathematical representation that illustrates the UAV kinematics and dynamics. It comprises the development of the UAV Equations of Motion that contains the aerodynamic forces and moments [21]. The UAV axes are right-handed. The *x*-axis is perpendicular to the *z*-axis and to the North. The *y*-axis is perpendicular to the *xz*-plane to the East. Figure 1 shows TVC-AV total forces and moments. Moreover, the UAV orientation (yaw, pitch and roll).

2.1. *Kinematic model*

The kinematic model is represented in two equations that relate the linear and angular positions in the inertial frame with those of the body frame and frame transformation matrices. In this model, forces and moments are not considered.

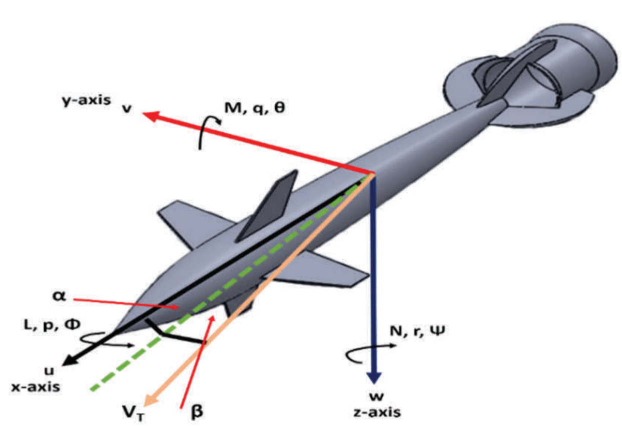

Fig. 1. The TVC-AV forces, moments, and orientations.

2.1.1. *Linear motion*

The linear velocities described in the body frame (u, v, w) can be related to the derivate of linear position in the inertial frame (p_n, p_e, p_d) through this equation:

$$\frac{d}{dt}\begin{pmatrix} p_n \\ p_e \\ p_d \end{pmatrix} = R_b^i \begin{pmatrix} u \\ v \\ w \end{pmatrix}, \tag{1}$$

where R_b^i is the transformation matrix from the body to the inertial frame.

2.1.2. *Angular motion*

The angular motion model represents the relation between the body angular rates, which is described in the body frame (p, q, r), and the angular positions (φ, θ, ψ), which is rotated with these angles around the body frame axis.

$$\begin{pmatrix} \dot{\varphi} \\ \dot{\theta} \\ \dot{\psi} \end{pmatrix} = R_b^r \begin{pmatrix} p \\ q \\ r \end{pmatrix}, \tag{2}$$

where R_b^r Is the transformation matrix from the frames that rotate around the body frame axis to body frame.

2.2. ***Dynamic model***

To develop the dynamic model, Newton's second law is applied to both translational and rotational motion. These equations have to be solved in a fixed frame, like the Earth frame, which is suitable for AVs and is used in this study. Consequently, the motion of AVs is transformed from the body frame to the Earth one by using rotational matrices [22].

2.2.1. *Translational motion*

Applying newton's second law:

$$\sum F = \frac{d}{dt_i}(\text{linear momentum}) = m\dot{V}_i, \tag{3}$$

where

F The summation of weight, propulsion, and aerodynamics forces that act on the AV.

m Body mass.

$\dot{V}_i$ The derivative of velocity in the inertial frame.

Because the forces that are applied on the body are in the body frame, Eq. (1) has to be translated to the body frame:

$$\sum F_b = m\dot{V}_b + w_{b/i} \times V_b, \tag{4}$$

$$F_b \equiv (f_x, f_y, f_z), \quad V_b \equiv (u, v, w), \quad w_{b/i} \equiv (p, q, r).$$

Hence, we get the translational equations:

$$\begin{pmatrix} \dot{u} \\ \dot{v} \\ \dot{w} \end{pmatrix} = \begin{pmatrix} rv - qw \\ pw - ru \\ qu - pv \end{pmatrix} + \frac{1}{m}\begin{pmatrix} f_x \\ f_y \\ f_z \end{pmatrix}. \tag{5}$$

2.2.2. *Rotational motion*

Applying newton's 2nd law,

$$\sum M = \frac{d}{dt_i}(\text{angular momentum}) = \frac{dH}{dt_i}, \tag{6}$$

M is the moment that applied on the AV.

By transforming this moment from the inertial frame to the body frame, we get

$$\sum M_b = \frac{dH_b}{dt} + w_{b/i} \times H_b, \tag{7}$$

H_b The angular momentum presents the product of the angular velocity and inertia matrix.

$$H_b = Jw_{b/i}. \tag{8}$$

Substitute from (6) in (5), then

$$\sum M_b = \frac{dJw_{b/i}}{dt} + w_{b/i} \times Jw_{b/i}, \tag{9}$$

$$\dot{w}_{b/i} = J^{-1}[-w_{b/i} \times (Jw_{b/i}) + M], \tag{10}$$

$$\dot{w}_{b/i} = \begin{pmatrix} \dot{p} \\ \dot{q} \\ \dot{r} \end{pmatrix}, \quad J = \begin{pmatrix} j_{xx} & j_{xy} & j_{xz} \\ j_{yx} & j_{yy} & j_{yz} \\ j_{zx} & j_{zy} & j_{zz} \end{pmatrix},$$

for the body symmetry about their two planes, then the product of inertia is very small and can be assumed to be zero

$$J = \begin{pmatrix} j_{xx} & 0 & 0 \\ 0 & j_{yy} & 0 \\ 0 & 0 & j_{zz} \end{pmatrix}. \tag{11}$$

Equations (1), (2), (5), and (10) describe the AV's dynamic model; however, it is incomplete because it does not consider the external forces and moments, such as gravity, aerodynamic forces, and propulsion.

2.3. ***Aerodynamic mathematical representation***

Aerodynamics describes how air impacts the behavior of a flying vehicle. This involves determining aerodynamic coefficients and derivatives to calculate the resulting aerodynamic forces and moments. These forces and moments are categorized into two main components: longitudinal and lateral. Longitudinal components affect translational motion in the *x*-*z* plane and rotational motion in the pitch plane, while lateral components influence side-to-side translational motion and rotational in roll and yaw [23].

2.3.1. *Aerodynamic longitudinal component*

The aerodynamic longitudinal component includes lift and drag forces as well as pitching moments. These forces are produced in the wind frame and depend on the angle-of-attack (α). Therefore, lift, drag, and pitching moments can be determined using the following calculations:

$$L = \frac{1}{2}\rho V_{av}^2 S C_L, \tag{12}$$

$$D = \frac{1}{2}\rho V_{av}^2 S C_D, \tag{13}$$

$$m = \frac{1}{2}\rho V_{av}^2 S c C_m, \tag{14}$$

where

S Reference area
c Wing mean chord
ρ Air density,
V Cruise velocity.

C_L, C_D, and C_m are coefficients representing lift, drag, and pitching moments, respectively. They are nonlinear but can be linearized through Taylor series approximations and decomposed into fundamental aerodynamic coefficients and derivatives [24].

2.3.2. *Aerodynamic lateral component*

The aerodynamic lateral component includes side force as well as roll and yaw moments. These forces and moments affect the lateral movement of the AV within the wind frame and are dependent on the sideslip angle (β). They can be expressed as follows:

$$Y = \frac{1}{2}\rho V_{av}^2 S C_Y, \tag{15}$$

$$l = \frac{1}{2}\rho V_{av}^2 S b C_l, \tag{16}$$

$$n = \frac{1}{2}\rho V_{av}^2 S c b C_n, \tag{17}$$

b Reference length
C_Y, C_l, and C_n are side, roll, and yaw aerodynamic coefficients. Also, they are divided into basic and derivatives coefficients after linearization is performed [24].

3. Modeling of Thrust Vectoring

As illustrated in Fig. 2, there are two coordinate frames: the body frame, which has been previously described, and the thrust frame, which is used to define the thrust vector along the three axes. The origin of the thrust frame is located at the center of the nozzle (the center of the thrust output plane). The *X*-Thrust and *X*-Body axes are aligned and identical, while the *Y*-Thrust and *Z*-Thrust axes are parallel to the *Y*-Body and *Z*-Body axes, respectively.

In the typical scenario where the vehicle is moving forward, the exhaust direction is opposite to the X-Thrust (X-Body) direction. However, if the joint nozzle is rotated within the ZX or XY plane, force components are generated in these planes. These forces create moments around the center of gravity (CG), which induce pitch and yaw rotations of the body.

The values of the force components will depend on the τ and η angles that describe the deflection of the thrust from the *X*-Thrust and the *Y*-Thrust. The value of the force in the three axes can be described as follows:

$$F_x = F\cos(\tau) + F\sin(\eta), \tag{18}$$

$$F_z = F\sin(\tau), \tag{19}$$

$$F_y = F\cos(\eta), \tag{20}$$

where τ represents the angle between the *X*-thrust axis and the direction of thrust in the *ZX* plane. η is the angle between the *Y*-thrust axis and the direction of thrust in the *XY* plane. F denotes the magnitude of the motor thrust. According to Newton's third law, which states that for each action there is an equal and opposite reaction, the direction of the exhaust will be opposite to the *X*-thrust direction, making the thrust force act in the reverse direction of the exhaust.

The value of F_x represents the thrust force that propels the body forward. As indicated by the equations, during gimbaling, the forward thrust value will decrease. Since F_x aligns with the center of gravity (CG), it does not create a moment. However, F_y and F_z, which do not pass through the

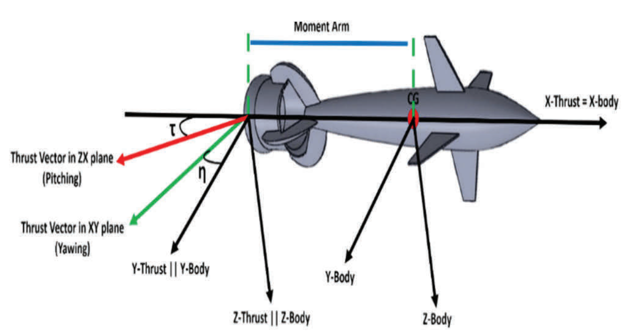

Fig. 2. The TVC mathematical model.

CG, generate a moment around the CG. This moment can be described as follows:

$$M_y = F_z * \text{Moment Arm}, \tag{21}$$

$$M_z = F_y * \text{Moment Arm}, \tag{22}$$

where M_y is the moment of F_z, which made the body rotate around the y-body.

M_z is the moment of F_y, which made the body rotate around the z-body.

As mentioned before, as the value of F_x passes with the center of gravity, it will not produce moment so the canard surfaces will be used to control the roll motion.

M_y represents the moment generated by F_z, which causes the body to rotate around the Y-body axis. Similarly, M_z denotes the moment produced by F_y, which causes rotation around the Z-body axis.

As previously mentioned, since F_x passes through the center of gravity, it does not create a moment. Therefore, canard surfaces will be employed to control roll motion.

4. Modeling of the TVC-UAV Case Study

The integration of AV sub-models results in a comprehensive 6-DOF nonlinear model. This nonlinear model is developed to create computer programs that can solve the mathematical equations governing AV flight dynamics, which involve the forces and moments experienced during flight. The AV's geometric model is detailed, the mass inertia model is determined through experimental methods, and the aerodynamic model is approximated using a semi-empirical, CFD approaches, and wind-tunnel experiments [25]. The actuation model is estimated through system identification based on experimental data. Additionally, the atmospheric model is constructed according to ISA standards, and the AV's electric propulsion system is also modeled using identification techniques. A MATLAB® (Simulink) model is then developed using data gathered from all these sub-models [26].

4.1. *Geometric model*

Figure 3 illustrates the geometric shape of the body under test, which comprises three sections: the canard section, the fuselage, and the rear section. As previously noted, this study employs the ball-joint method to adjust the vehicle's direction in pitch and yaw motions. Given that the vehicle utilizes a single engine, it may not be capable of generating rolling moments. To address this limitation, four canard surfaces will be used to facilitate rolling motion, as depicted in Fig. 3 of the body.

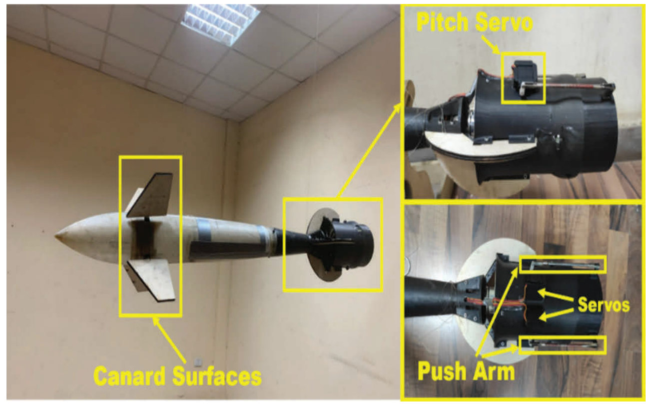

Fig. 3. The TCV-AV geometry with the TVC unit.

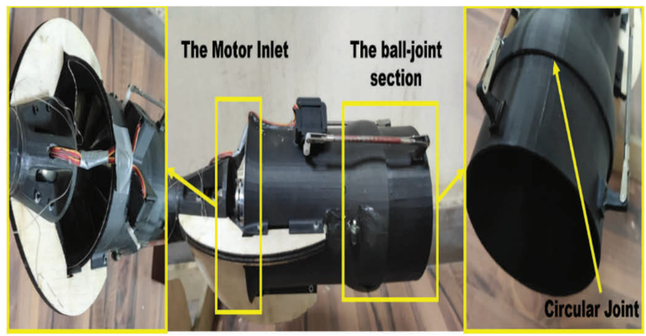

Fig. 4. The TVC unit.

The Ball-Joint Thrust Vector Control (BJ-TVC) is regarded as the most practical solution due to its extended operational life, improved energy efficiency, minimized thrust loss, and reduced maintenance expenses. Generally, the dynamics of these systems are represented using a universal gimbal joint mechanism, which frequently ignores uncertainties like the vertical displacement of the nozzle's pivot point [27].

Figure 4 illustrates the real section (TVC section), where push rods will be used as transmission levers to convey the motion of the servo to the joint section. This adjustment modifies the thrust vector, allowing it to deflect the body in the opposite direction. The propulsion system used in this work is an electric motor to avoid issues related to fuel and variations in the center of gravity (CG), which can affect the vehicle's attitude. Additionally, the capacity of the battery is a crucial parameter influencing both thrust and vehicle endurance. As the size of the vehicle increases, its weight also increases, which in turn reduces the payload capacity.

All geometric data for the body are measured to completely develop the geometric model, as presented in Table 1.

Table 1. The geometric data.

Property	Value
Nose length (cm)	30
Canard root chord length (cm)	12
Canard tip chord length (cm)	6
Canard semi-span length (cm)	12
Fuselage length (cm)	1200
Body diameter length (cm)	10
Canard airfoil	NACA 0006

4.2. *Mass-inertia model*

The UAV under-test has a symmetrically distributed mass about the x-z and x-y planes. So, the products of inertia $I_{zy}, I_{xy}, I_{yz}, I_{yx}$, and I_{zx} can be neglected. The UAV moments of inertia could be estimated from the CAD tool. Also, these results are verified by experimental measurements using the pendulum method. It is an easy and cheap method to estimate accurate results for small UAVs.

It is important to mention that the inertia model, while validated through these experimental methods, cannot be perfectly accurate based solely on simulations or calculated estimations. In practice, experimental determination is essential to ensure that the inertia properties are fully representative of the vehicle's real-world behavior. Therefore, we conducted several rounds of physical testing on our prototype to further refine and validate the inertia properties, especially as part of our validation process.

These experiments are performed on loaded UAVs with all their components. UAV is hinged as shown in Fig. 5. Each position is used to estimate the moment of inertia about each axis. The setup and procedures are as follows:

4.2.1. *Set up the pendulum experiment*

- The UAV is treated as a pendulum and swung about a rotational axis.
- The symmetry of the UAV allows neglecting certain inertia terms (e.g. products of inertia like $I_{zy}, I_{xy}, I_{yz}, I_{yx}$, and I_{zx}).

4.2.2. *Ensure conditions for the experiment*

The oscillation must occur in the vertical plane containing the arm of the pendulum and perpendicular to the axis of rotation with these considerations.

- Small Oscillation Amplitude: As shown in Fig. 5, the initial displacement angle (θ) should be small enough to satisfy the condition ($\sin(\theta) \approx \theta$) and ($\tan(\theta) \approx \theta$), where θ is the angle of displacement that lies in the range between 10° and 15° and the frequency of oscillation is determined about each axis ω_n, and by using the described formula in [17] the moment of inertial is directly calculated.
- Length of Suspension: For UAVs weighing less than 5000 pounds, the distance between the point of suspension and the UAV's center of gravity (CG) should range from 4 to 6 feet.

4.2.3. *Conduct multiple tests for accuracy*

Perform the pendulum experiment five times for two different lengths of suspension (short and long) and take the average to improve accuracy.

4.2.4. *Calculate the moment of inertia*

The equation of motion for a simple pendulum provides the formula to estimate the moment of inertia (MOI) of the

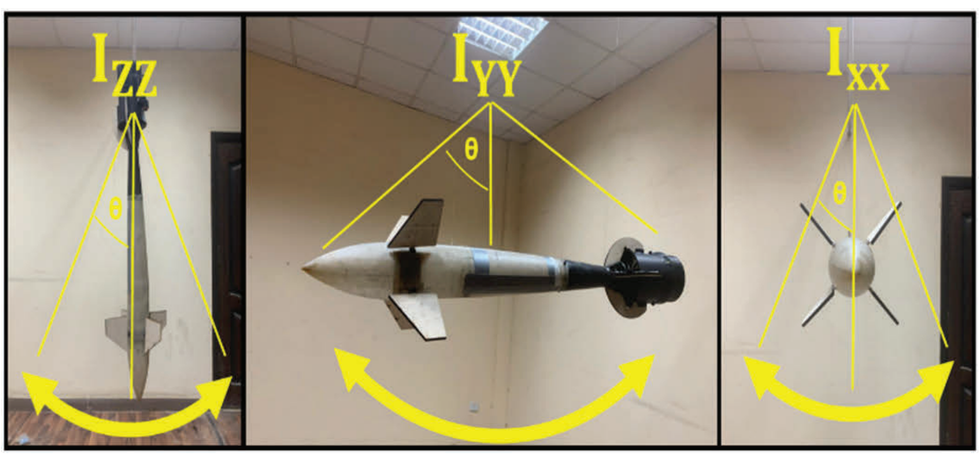

Fig. 5. The UAV moment of inertia experiment's setup.

UAV. The general equation is

$$I_{\mathrm{CG}} = \frac{mgL_{\mathrm{C.G}}}{\omega_n^2} - mL_{\mathrm{C.G}}^2, \tag{23}$$

where

m is the UAV total mass. $L_{C.G}$ is the distance from the fixed point to the UAV center of gravity.

g is acceleration due to gravity.

ω_n is the natural frequency of UAV oscillation and can be calculated by $\sqrt{\mathrm{Re}^2 + \mathrm{Im}^2}$.

I_{CG} = Moment of Inertia about the center of gravity for CG plane.

The UAV's swinging motion can be represented as damped oscillation. The real (Re) and imaginary (Im) components of this oscillation determine the natural frequency of oscillation (ω_n), the real part of the natural frequency is$\mathrm{Re} = (5/T_f)$, while the imaginary part is $\mathrm{Im} = (2\pi/T)$, where T_f is the time taken for oscillation to damp out and T is the swinging time of one oscillation.

In these experiments, the UAV is fully assembled with all components and hinged as shown in Fig. 5. Moments of inertia are estimated for each axis by observing the UAV's oscillation from various positions. The body is displaced with a small angle, about five degrees, from its rest position. Then it is released and allowed to oscillate freely. Ten oscillations are counted and their swinging time is recorded as well as T_f. The MOI is then calculated directly using the formula provided in Eq. (22).

This process is applied multiple times for each axis to determine the average values. Oscillations are measured in the roll, pitch, and yaw planes. The moments of inertia of each swing about the three axes derived from these experiments are presented in Table 2.

The moment of inertia, as estimated using the ANSYS tool, is presented in Table 3, utilizing the same meshing network employed for the aerodynamic analysis. Additionally, the standard deviations have been calculated, and the referenced values are derived from experimental tests.

It is important to mention that while simulations and analytical calculations provide valuable estimates, they can never fully replace experimental testing when it comes to accurately determining inertia properties.

The calculated standard deviations for the given sets of actual and simulated values indicate that the simulations can be relatively accepted, however, the experimental results remain the most reliable for utilization since these measurements are typically more trusted due to their direct measurement of physical properties and can be considered the more Credible reference for the moment of inertia. So, in this work, the experiment measurements will be used.

Table 2. The values of each swing about the three axes.

Test no.	No. of oscillation	Total time of oscillation	Moment of inertia
Inertia test I_{xx}			
1	10	27	0.362
2	10	26	0.312
3	10	27	0.328
4	10	25	0.337
5	10	27	0.386
Average	10	26.4	0.345
Inertia test I_{yy}			
1	10	22	0.723
2	10	22	0.767
3	10	24	0.772
4	10	21	0.721
5	10	21	0.747
Average	10	22	0.746
Inertia test I_{zz}			
1	10	23	0.894
2	10	22	0.881
3	10	21	0.849
4	10	22	0.858
5	10	22	0.898
Average	10	22	0.876

Table 3. The moments of inertia.

Moment of inertia	Experimental values	Ansys CAD tool	Standard deviations
I_{xx}	0.345	0.265	0.04
I_{yy}	0.746	0.637	0.0545
I_{zz}	0.876	0.926	0.025

4.3. *Actuator model*

The actuation system is used to steer the body to the desired position based on control commands received or generated by the autopilot. The angle achieved by the actuator should align with the required angle, according to its dynamics. Understanding these dynamics is crucial to accurately assess the vehicle's behavior.

System identification is a technique used to create mathematical models of dynamic systems by analyzing measurements of input and output signals [28]. This process involves testing various model structures to find the best-fitting model. Once a model is selected, validation data are used to confirm its accuracy and suitability. Figure 6

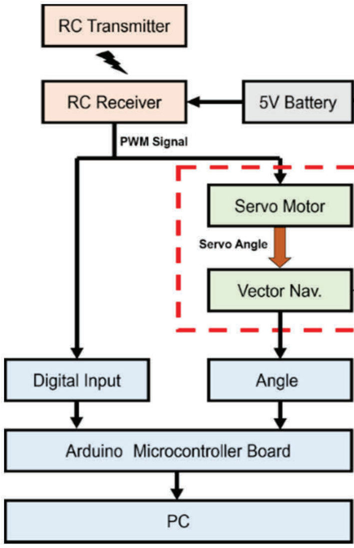

Fig. 6. Block diagram for the servo-motor identification experiment.

shows the block diagram for the servo-motor identification experiment.

The system involves six servos: four are responsible for rolling motions via canards, and the remaining two handle pitch and yaw through the thrust vector control (TVC) unit. For system identification, one servo from each type (canard and TVC) is identified since they have identical specifications. The hardware setup comprises a PC running MATLAB® (Simulink) that processes input angles and feedback angles from the servos. An Arduino-Uno generates PWM signals based on the required angles from MATLAB® (Simulink) to control the servos, and a Vector-Nav sensor measures and relays the achieved angles back to the toolbox.

In the System Identification Toolbox, a black-box modeling approach is used, starting with simple linear models and progressing to more complex ones if needed. The models are refined through trial and error to achieve the best fit. Input and output signals for step inputs are analyzed, and both linear and nonlinear models are tested. Validation data with various step inputs are used to compare the performance of these models.

The UM7 orientation sensor measures the servo angle deflection and serves as an Attitude and Heading Reference System (AHRS). It integrates data from a three-axis accelerometer, a rate gyro, and a magnetometer using an Extended Kalman Filter to provide estimates of attitude and heading. Only one accelerometer is used, aligned with the servo horn. Additionally, a dummy weight is attached on the servo horn to simulate the pressure on the servo during flight to closely replicate real dynamics. Figure 7 shows the identification process of the servo that was used for the canard deflection.

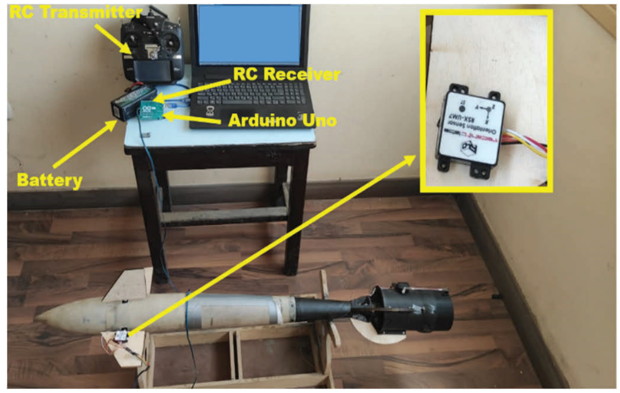

Fig. 7. System identification setup for the canard actuation.

As shown in Figs. 8 and 9, the canard servos models based on the Nonlinear Auto-Regressive with External Input (NLARX) model provided a fit value of 91.8%, though it showed some overshoot (the red circles). The Output Error (OE) model, with an 82.78% fit, was considered acceptable. First and second-order transfer functions achieved fit values

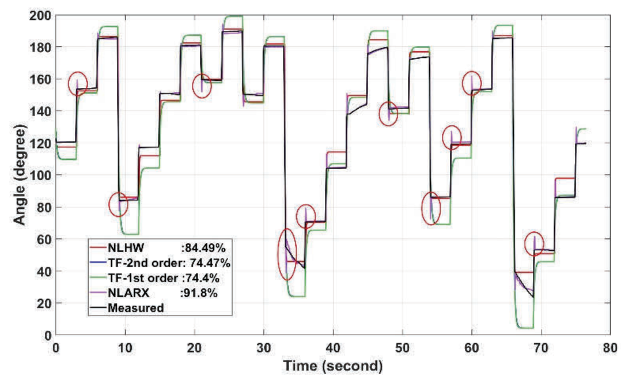

Fig. 8. Linear and nonlinear models of canard.

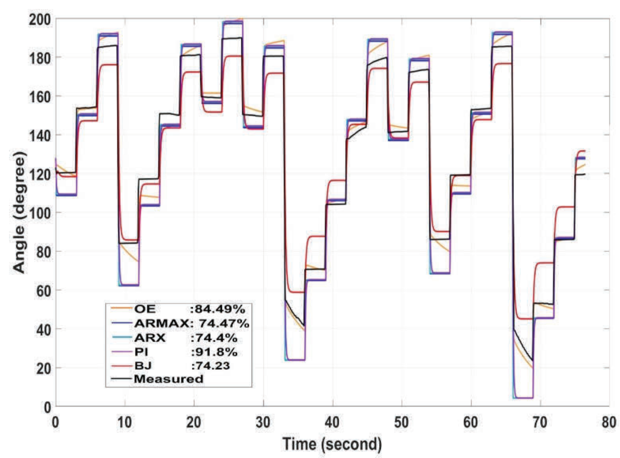

Fig. 9. Linear polynomial and process models of canard.

of 74.47% and 74.4%, respectively, which are acceptable for small UAVs. These transfer functions are used in MATLAB® (Simulink) to control both canard and TVC servos.

Figure 10 shows the identification setup of the servo used for the TCV, designed to analyze and determine its dynamic behavior. This process involves applying known input signals to the servo and measuring its output response. By studying the time-domain response, key parameters, such as gain, time constants, and damping ratios can be identified, these parameters are essential for building an accurate model of the servo's performance, which is crucial for optimizing control strategies in systems like the TCV (Throttle Control Valve) or UAVs.

The identification setup helps ensure precise control and reliability in dynamic systems by accurately capturing the servo's characteristics.

As shown in Figs. 11 and 12, For TVC servos, the NLARX model achieved an 83.03% fit value, and the first-order and second-order transfer functions achieved fit values of 67.23% and 67.02%, respectively, The OE model achieved an 80.13% fit value.

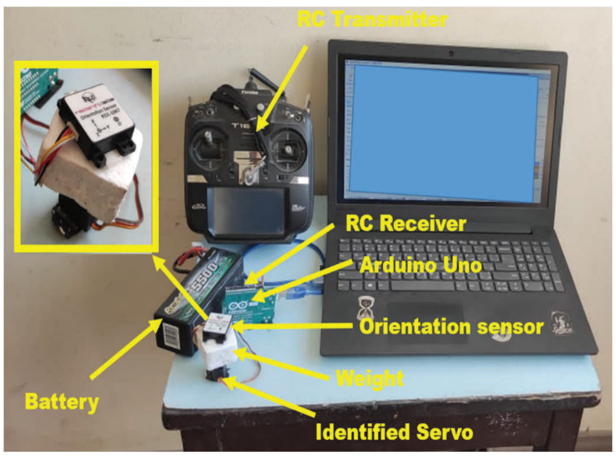

Fig. 10. System identification setup for the TVC actuation.

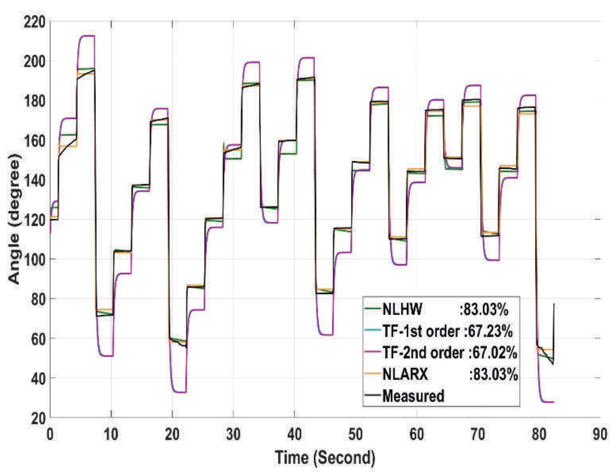

Fig. 11. Linear and nonlinear models of TVC.

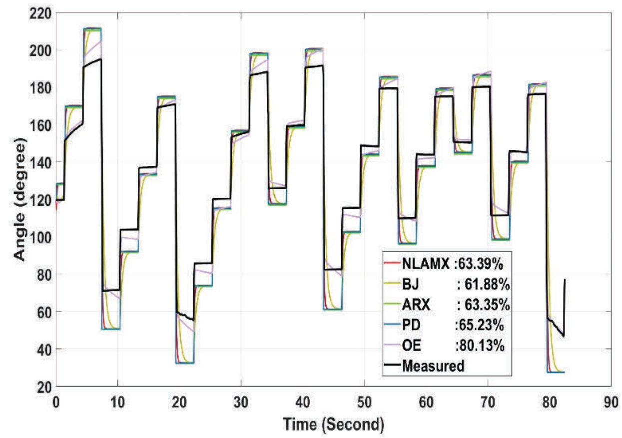

Fig. 12. Linear polynomial and process models of TVC.

The fit values for the identified models are summarized in Table 4.

4.4. *The aerodynamics*

The aerodynamic characteristics refer to the properties and behaviors of an aircraft or vehicle in response to airflow. These characteristics are crucial for understanding how aerodynamic forces impact the performance, stability, and control of the vehicle [29]. This work presents different approaches to estimate their characteristics using simulation software or experimental tests.

The use of different approaches for aerodynamic analysis, such as semi-empirical techniques, computational fluid dynamics (CFD), and wind-tunnel experiments, is essential because each method offers distinct advantages and can be used to address different aspects of aerodynamic behavior. Here's why a combination of these methods is often employed:

- **Semi-Empirical Techniques**

Advantage: These methods are typically faster and less computationally intensive than CFD or wind-tunnel testing. They rely on empirical data and simplified mathematical models to estimate aerodynamic characteristics.

Use: Ideal for quick estimates or for cases where full simulation or experimental testing is not feasible, such as during the initial design phase of a vehicle or UAV.

Limitation: Semi-empirical methods may not capture the full complexity of airflow dynamics, especially in cases involving complex geometries or extreme flight conditions.

Table 4. Servo models fitting percentage.

	Linear models (Transfer function)		Nonlinear model		Linear models Nonlinear model				
Type of models	1st order	2nd order	NLARX	NLHW	ARX	ARMX	BJ	OE	Process model
Canard servo	74.4%	74.47%	91.8%	84.49%	71.31%	71.01%	74.23%	82.78%	PI (72.13%)
TVC servo	67.23%	67.02%	83.03%	83.03%	63.35%	63.39%	61.88%	80.13%	PD (65.23%)

- **Computational Fluid Dynamics**

Advantage: CFD simulations provide a detailed, high-fidelity analysis of aerodynamic flow around the vehicle. They can model complex geometries and predict forces like drag, lift, and moments across a wide range of conditions (e.g. different angles of attack and Mach numbers).

Use: Ideal for in-depth analysis, optimization, and fine-tuning of the aerodynamic design. CFD is particularly useful when dealing with complex flow phenomena (such as turbulence or shockwaves) that are difficult to model with simpler approaches.

Limitation: CFD simulations can be computationally expensive and time-consuming, especially for complex geometries or high-fidelity simulations.

- **Wind-Tunnel Experiments**

Advantage: Wind tunnels provide real-world, experimental data about aerodynamic performance, offering a high degree of reliability. These experiments allow for direct measurement of forces and moments on a physical model of the vehicle.

Use: Wind-tunnel tests are critical for validating simulation results and for refining designs before physical production. They offer insights that can't always be captured through CFD, such as issues with surface roughness or unanticipated flow phenomena.

Limitation: Wind-tunnel testing can be expensive, time-consuming, and may not perfectly replicate real-world conditions (e.g. full-scale flight dynamics). Additionally, scaling effects might introduce errors in testing small models.

- **Why Use Different Approaches?**

Complementarity: Each method has its strengths and limitations, so combining them helps overcome the weaknesses of any one method. For example, CFD can provide detailed insights that semi-empirical methods might miss, while wind-tunnel testing validates CFD results and provides real-world data.

Accuracy vs. Practicality: Sometimes, high accuracy (from CFD or wind-tunnel testing) is not required for early design stages, so simpler semi-empirical methods are used. Conversely, when precise, high-fidelity results are needed (e.g. for flight testing or final design validation), CFD and wind tunnels are more suitable.

Cost and Time Efficiency: While wind-tunnel tests can be expensive and time-consuming, they provide real-world validation that can confirm or refute the results from CFD or semi-empirical models. Using a mix of approaches can help balance cost, time, and the need for accuracy.

4.4.1. *The semi-empirical approach*

The aerodynamic characteristics of the UAV are estimated using the Dynamic Aero-elasticity and Control (DATCOM) tool, DATCOM is a semi-empirical tool used for estimating aerodynamic characteristics. It is particularly useful for small UAVs and low-speed flight conditions. It generates aerodynamic coefficients and derivatives based on the UAV's shape and flight conditions.

The DATCOM input file is created by detailing the UAV's geometric and flight parameters. This includes information about the UAV's shape, size, and flight conditions (e.g. speed, altitude). And the data include the geometry of the UAV (such as surface shape and size) and the conditions under which it is flying.

The DATCOM provides basic aerodynamic coefficients and their derivatives such as lift, drag, and pitching moment coefficients. These coefficients are essential for understanding how the UAV will perform in different flight conditions [30]. The coefficients are tabulated in lookup tables. These tables store data for different angles of attack and other relevant parameters, which are used to build the aerodynamic model.

The lift curve in Fig. 13 shows how the lift coefficient (CL) changes with the angle of attack (α). As α increases, the lift coefficient generally increases until it reaches the stall angle (α_{stall}) at which the lift coefficient reaches its maximum and starts to decrease, indicating that the flow has separated from the wing surface.

The drag coefficient (CD) also increases with α. This increase is due to the growing aerodynamic drag as α increases as shown in Fig. 14, which affects the UAV's performance.

Figure 14 presents the values at speeds of 10, 20, 30, 40, and 50 m/s.

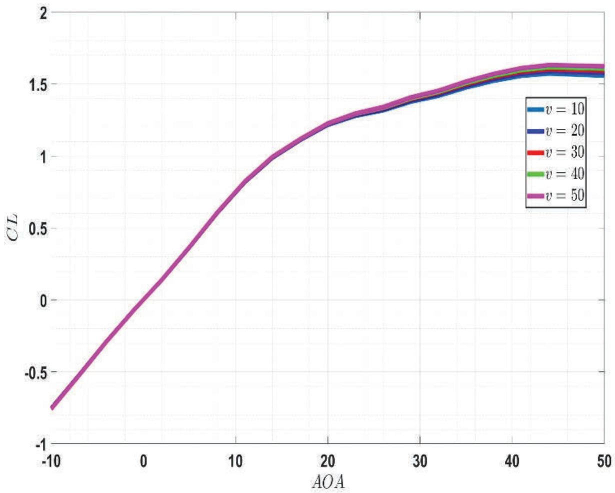

Fig. 13. The lift coefficient vs. the angle-of-attack.

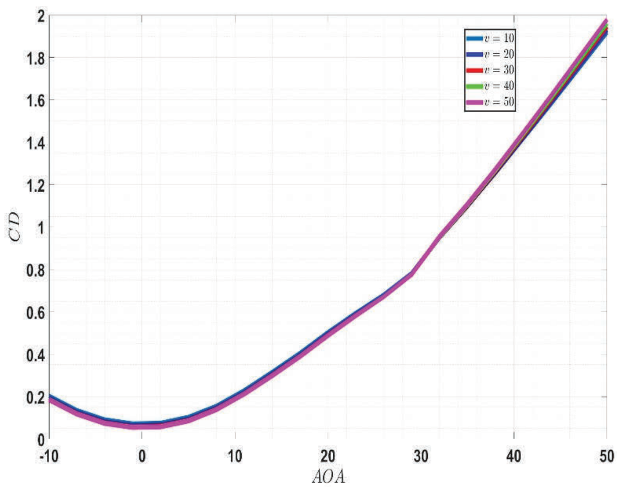

Fig. 14. The drag coefficient vs. The angle-of-attack.

Figure 15 shows the pitching moment coefficient (Cm) that indicates how the UAV's nose will pitch up or down. As α increases, the pitching moment coefficient typically decreases, which affects the UAV's stability and control.

As illustrated in Fig. 16, the maximum values of the lift-to-drag ratio (CL/CD) do not exceed 5 primarily because the body geometry lacks a dedicated lifting surface such as a wing. Despite the absence of a wing, the lift force generated by the dynamic pressure on the body is sufficient to achieve lift force.

Figure 17 aids in identifying the optimal flight angle of attack (α) for the UAV, a critical parameter for maximizing aerodynamic performance. At this optimal angle, the lift coefficient reaches its maximum value, while the drag coefficient is minimized. This balance between lift and drag is essential for achieving the best possible combination of

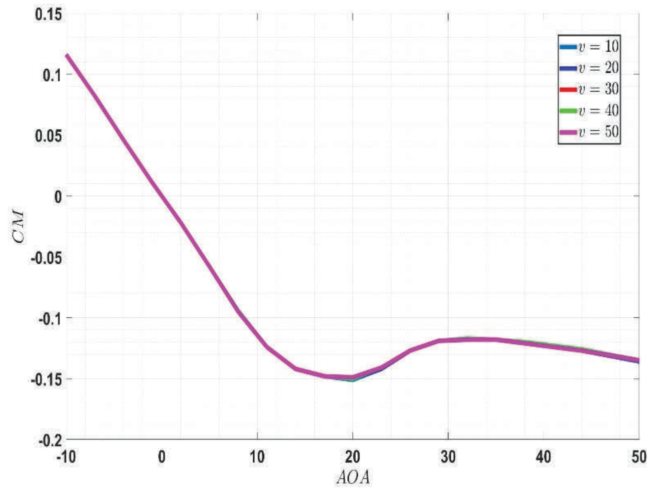

Fig. 15. The pitch moment coefficient vs. the angle-of-attack.

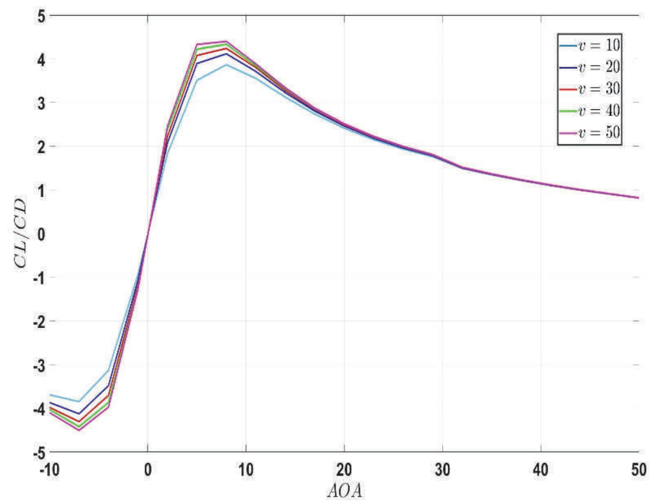

Fig. 16. The CL/CD vs. The angle-of-attack.

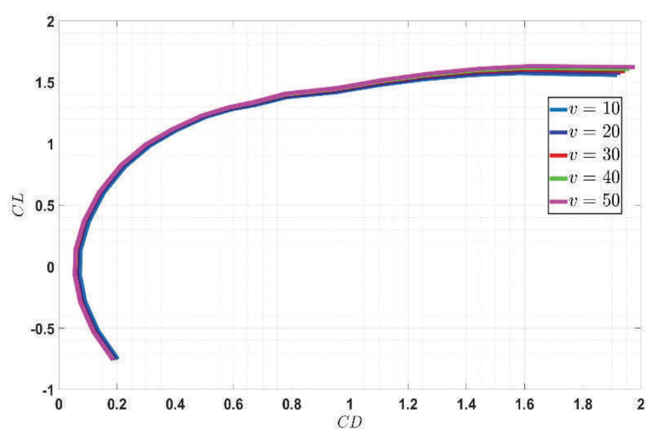

Fig. 17. The lift coefficient vs. the drag coefficient.

performance and efficiency during flight. Maximizing lift enhances the UAV's ability to stay aloft while minimizing drag reduces power consumption and improves overall flight endurance. Understanding and selecting the optimal angle of attack ensures that the UAV operates efficiently, leading to improved mission success and reduced operational costs.

The optimal lift-to-drag ratio is achieved at α of 8°, where the body exhibits a favorable balance of high lift and low drag.

4.4.2. *The computational fluid dynamics*

Because of the limited accuracy of DATCOM results, the Computational Fluid Dynamics approach using ANSYS software will be employed for validation. ANSYS software is known for its high validation accuracy, achieving up to 95% of real values. However, it requires substantial processing time, which can extend to several days, and demands significant hardware resources, making it impractical for all stages of the design process. Therefore, DATCOM will be utilized during the preliminary design phase, offering around 75% accuracy [31], while ANSYS will be reserved for the final stage to ensure the validation of results.

Most of the flow analyses conducted on the UAV have been performed using numerical techniques through CFD. The software generates calculations primarily based on the Reynolds Averaged Navier-Stokes (RANS) equations. These equations are governed by fundamental principles including continuity, momentum, energy, and turbulence, while accounting for viscous effects and boundary layer conditions. The outcomes of these calculations yield various flow parameter contours over the UAV's body [32].

In all the experiments utilizing numerical methods, it has been noted that the primary advantage of these techniques is their ability to provide accurate results for new or optimized designs without the necessity of physical test setups. Prior to running any analysis, it is essential to develop a precise model that accurately replicates real-world conditions to ensure the validity of the results [33].

The standard procedure for CFD computations begins with the creation of an appropriate mesh, once the mesh is established, boundary conditions are applied according to the operating environment of the object or body under investigation. Initial calculations are informed by previous experiments to serve as a reference for subsequent analyses.

This approach allows for the derivation of valid conclusions through the solution graphs and contours obtained. The governing equations used in CFD calculations are based on these fundamental principles [34].

- Continuity Equation (Conservation of Mass):

$$\frac{\partial \rho}{\partial t} + \nabla.(\rho u) = 0, \tag{24}$$

where ρ is the fluid density and u is the velocity field.

- Momentum Equation (Conservation of Momentum):

$$\frac{\partial(\rho u)}{\partial t} + \nabla.(\rho u u) = -\nabla p + \nabla.(\mu(\nabla u + (\nabla u)^T)) + f, \tag{25}$$

where p is the pressure, μ is the dynamic viscosity, and f represents external forces such as gravity.

- Energy Equation (Conservation of Energy):

$$\frac{\partial(\rho E)}{\partial t} + \nabla.(\rho u E) = -\nabla.q + \Phi, \tag{26}$$

where E is the total energy per unit mass, q is the heat flux vector, and Φ represents viscous dissipation.

The CFD involves three key stages: pre-processing to set up the model, numerical analysis to solve equations, and post-processing to interpret and present results. Figure 18 shows the CFD's main stages.

Each stage is crucial for accurate fluid flow simulations. As mentioned, the CFD process is divided into three main stages. The first stage, pre-processing, involves preparing all the necessary data for the solver. This includes creating a 3D model of the object, determining input parameters such as flow and thermal conditions, generating the mesh network, and setting up physical models and boundary conditions.

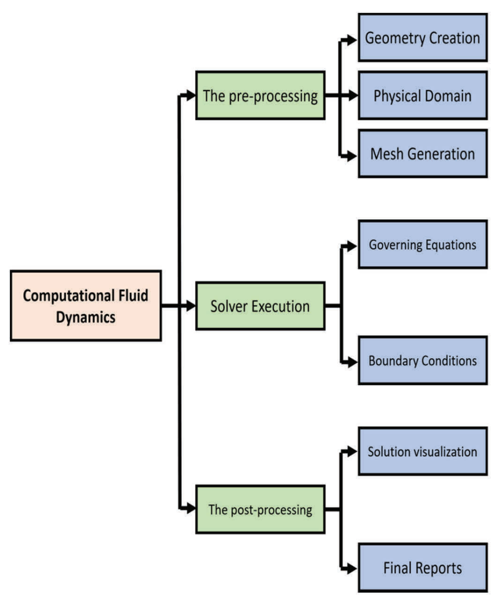

Fig. 18. The CFD's main stages.

The second stage is numerical analysis, where iterative partial differential equations are solved to obtain numerical solutions.

The final stage is post-processing, which focuses on analyzing and visualizing the results. This includes generating numerical graphs, visualizations, and compiling final reports that summarize the findings of the CFD analysis [35].

- ***Geometry Generation***

The model was initially created using SolidWorks and then imported into ANSYS with IGS format.

- ***Fluid Domain and Mesh Generation***

To accurately simulate the flow around the body, a fluid domain was established that extends 5L upstream, 8L downstream, and 5L around the model, where L represents the length of the UAV. For the flow analysis, a finite volume method was employed. The rectangular domain was meshed using unstructured grid elements. This process included face meshing for each surface and defining edge sizes for the number of divisions, as illustrated in Fig. 19.

The quality of the mesh is assessed using mesh metrics to ensure that it maintains good orthogonality, aspect ratio, and skewness.

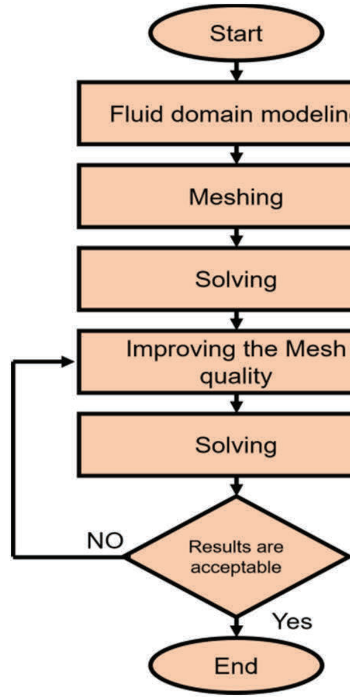

Fig. 20. Grid convergence study flow chart.

- ***Mesh Independence Study***

In CFD, Grid Convergence Studies (GCS), as shown in Fig. 20, are important and the best practice for validating computational results in the absence of an exact solution. While the exact error cannot be calculated, convergence is assessed by extrapolating results from a series of systematically refined grids toward an infinitely fine grid [36].

Our model was analyzed using six progressively refined grid approaches, and the results show that these refinements effectively enhanced the model's performance. This observation aligns with prior research, which has shown that gradual refinement of a model generally yields improved results.

The meshing was designed with very small elements to accurately capture all the curvature and sharp edges of the body. Additionally, an inflation layer (the inflation layer is a series of progressively smaller grid cells placed close to the surface of the object being analyzed, the thin region of air near the surface where the velocity changes from zero at the surface to the freestream velocity) was created around the body to enhance the simulation's accuracy by increasing the resolution and better capturing variations in velocity. Figure 21 shows the meshing inflation.

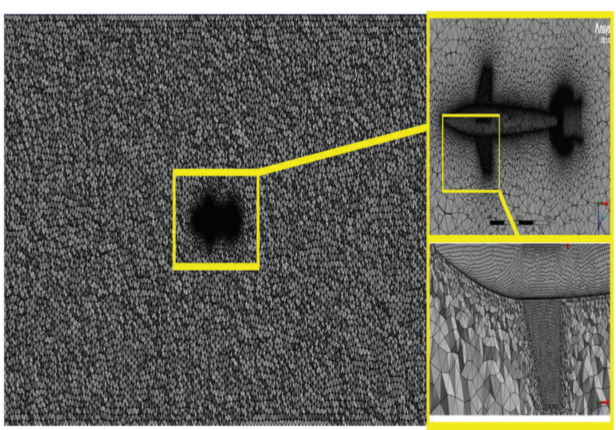

Fig. 19. The physical domain and mesh generation steps.

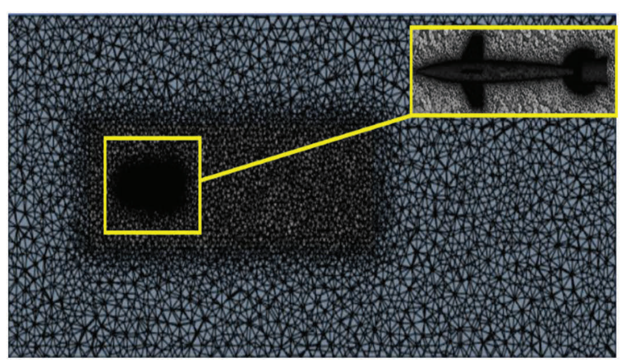

Fig. 21. The meshing inflation.

- ***Mesh Quality***

Mesh quality is evaluated using mesh metrics to ensure that orthogonality, aspect ratio, and skewness are optimized, as shown in Table 5, at velocity of 10 m/s and AOA of 5°, given the available computational resources.

Figure 22 shows the CFD of the flow over the model, the value of the flow is variation over the body and reaches its maximum value at the inlet and outlet of the propulsion system.

The CFD simulation has the ability to estimate the values of the pressure over the model to help in designing an internal structure design to avoid model deformation during the flight and estimate the weakest points in the design. Figure 23 shows the pressure (in Pascal) according to the flow. As seen, the maximum value of the air pressure is at the inlet of the propulsion.

Table 5. The mesh metrics.

Iteration	No. of elements	Aspect ratio	Skewness	Orthogonality	CL	CD
		Average	Average	Average		
1	2735342	1.983	0.35434	0.77348	0.98	0.45
2	3872987	1.736	0.29365	0.79935	0.45	0.34
3	4567823	1.568	0.22335	0.81256	0.84	0.31
4	5678263	1.287	0.19264	0.89762	0.75	0.22
5	6528764	1.123	0.11224	0.92827	0.74	0.23
6	8761673	1.023	0.01414	0.93546	0.74	0.23

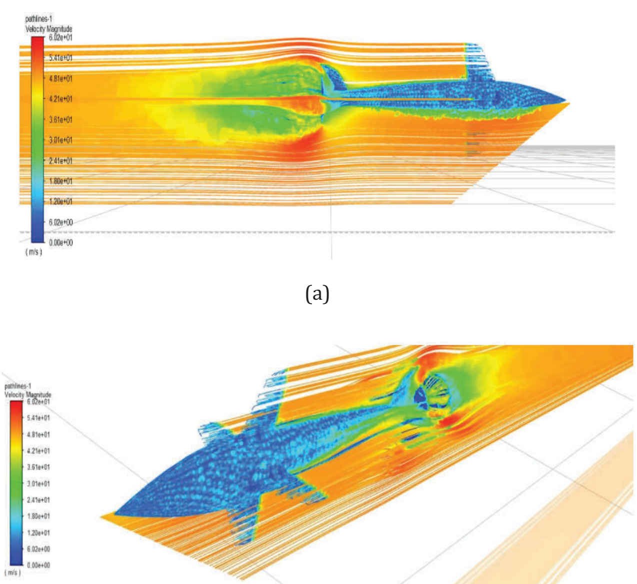

(a)

(b)

Fig. 22. The CFD simulation (a) 2D and (b) 3D.

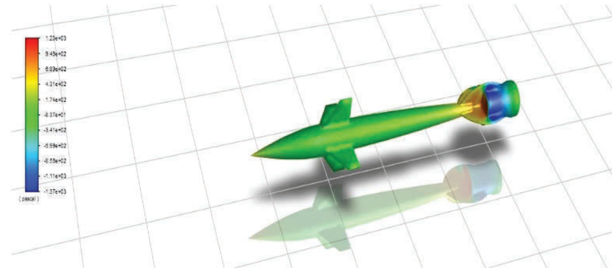

Fig. 23. The pressure simulation.

- ***Solver Setup***

In this paper, ANSYS Fluent was used as the solver to simulate the flow around a body at a Mach number of 0.146. To simplify the initial solution, we assumed an inviscid flow around the body that assumes that the viscosity of the fluid is negligible, meaning the effects of friction between fluid layers are ignored and this assumption can be employed for the low speed, This significantly reduces the complexity of the governing equations (Navier–Stokes equations), making the simulation more straightforward and faster to solve, especially for initial trials or preliminary studies.

Also, the velocity formulation is absolute, and the flow is considered steady, with no changes occurring after setting the initial boundary conditions for the governing equations. The energy equation and inviscid model were applied, with the density calculated based on the ideal gas law. Air was assumed as the fluid material [37].

4.4.3. *Wind-tunnel experiments*

The Wind tunnels provide accurate measurements of aerodynamic forces and moments on scaled models, offering precise data on lift, drag, and other key performance metrics. These data are essential for evaluating and enhancing the design of aircraft, vehicles, and structures. Additionally, wind-tunnel testing validates and calibrates CFD models, allowing for comparison with simulation results to improve accuracy and reliability. To ensure the experiment results, the experiment was installed using ready-made wind tunnel as shown in Fig. 24, and the experiments were implemented at AOA of 10° and 20°.

To address scaling effects in wind-tunnel testing, the Similarity Theory can be employed. This involves creating scaled models and applying factors like Reynolds number,

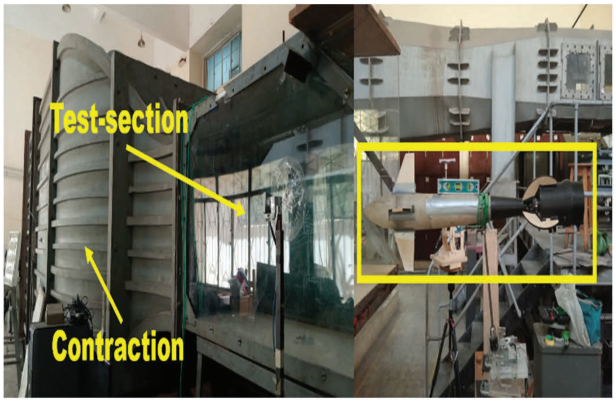

Fig. 24. The Wind-tunnel experiments.

Mach number, and geometric proportions to ensure the model's behavior accurately reflects that of the full-scale object in real-world conditions. This helps translate wind-tunnel results to full-scale performance. But, in this work, the full-scale prototype will be used so scaling factors are unnecessary for the following reasons:

- Real-world conditions: Testing the actual object at full scale means we are operating under the same conditions it was designed for, so no extrapolation from a model is needed.
- No model scaling: The aerodynamic forces, flow characteristics, and performance measured directly on the full-scale object will accurately reflect its true behavior in those conditions, without the need for a scaled model to predict performance.

Also, the limited size of the wind tunnel and wall effects can significantly influence the accuracy of full-scale wind-tunnel testing by introducing boundary layer disturbances, flow confinement, and possible flow separation near the walls. These effects can lead to distorted or nonrepresentative results, particularly in terms of pressure distribution, aerodynamic forces, and turbulence intensity. However, in this work, the model test section area is five times larger than the cross-sectional area of the model as the model under test doesn't contain a long-wing that reaches the wall like the common aerial vehicle shape. This small cross-section area significantly minimizes the potential influence of wall effects. This ample test section size ensures that the flow remains relatively uniform and that the wall effects are negligible. Furthermore, the measurement setup is fixed away from the direction of the airflow, meaning that the measurements are primarily influenced by the air pressure load on the surface of the model, rather than any distortion caused by the flow dynamics near the tunnel walls. As a result, the impact of wall effects on the test results can be considered minimal.

4.4.4. *Wind-tunnel implementation*

Due to the high cost associated with wind-tunnel experiments, this work presents a cost-effective method for designing a wind-tunnel and test unit (TU) to measure lift and drag coefficients for validating the simulations. As illustrated in the accompanying Fig. 25, the wind-tunnel structure includes a honeycomb section to obtain laminar flow. The design is optimized using CFD to achieve an air velocity of 10 m/s, constrained by the propulsion system. Four brushless motors from damaged quad-rotors are employed for this purpose.

The wind-tunnel design is divided into three sections: The first is the contraction section, which is critical for the design as it significantly affects the quality of the flow in the test chamber, this section is designed to accelerate the flow. The second section includes honeycombs intended to improve flow uniformity and reduce turbulence. Due to the complexity of implementing traditional honeycombs, this section is replaced with rectangular alternatives that aim to perform similar functions. The final section is the test section, where the test body is mounted for experimentation.

The tunnel structure is being constructed using wood, and the air flow system utilizes brushless motors, as previously mentioned, to minimize costs and utilize readily available tools.

Figure 26 shows the test unit that was implemented to measure the forces in the previous wind tunnel. The test unit for measuring lift and drag coefficients consists of a ban-tilt mechanism, two force cells, and a metal rod. The ban-tilt mechanism is utilized to rotate the body around the yaw and pitch axes, representing the tested angle of attack and side-slip angle, respectively. There are two force cells that measure the normal forces in the *Z*-direction and the axial force in the *X*-direction. The output from the force cells is amplified by a load cell amplifier before being transmitted to the embedded system for processing. Lift and drag coefficients are calculated using the relevant equations,

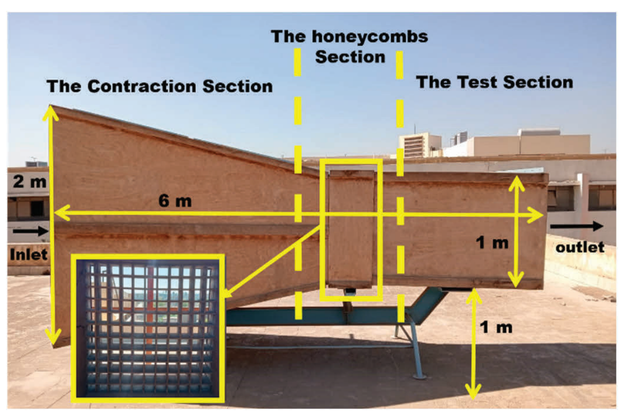

Fig. 25. The wind-tunnel implementation.

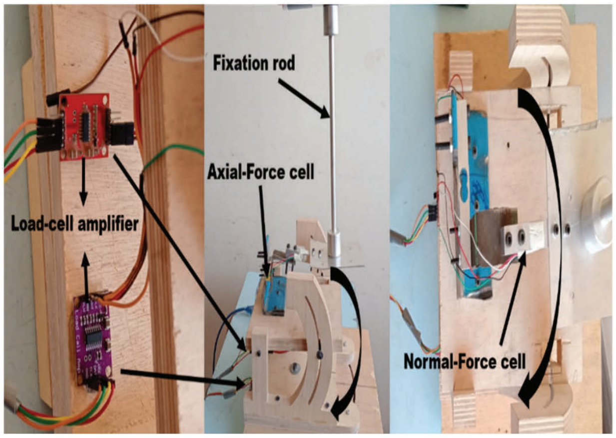

Fig. 26. The test unit of measuring lift and drag coefficients.

with θ corresponding to the tilt angle set during the experimental setup.

$$L = N\cos(\theta) - A\sin(\theta), \tag{27}$$
$$D = N\sin(\theta) + A\cos(\theta), \tag{28}$$

where

L is the lift force.

θ is the tilt angle

D is the drag force.

N is the normal force.

A is the axial force.

The force coefficient can be calculated as follows:

$$\mathrm{CL} = \frac{L}{\frac{1}{2}\rho v^2 S}, \tag{29}$$

where

S is the reference area ($S = \pi r^2$, r = 5 cm, which is the radius of the body).

V is the velocity of flow.

ρ is air density.

The metal rod is used to place the body on. The previous setup was constructed manually at a low cost and was employed to validate the values obtained from DATCOM and ANSYS software.

4.4.5. *Forces measurement using ground vehicle*

Due to limitations in airspeed, an additional experiment was conducted to measure coefficients at higher speeds. In this setup, the test unit and body were mounted on a ground vehicle as shown in Fig. 27. As illustrated in the accompanying figure, the vehicle traveled on a highly accurate road to minimize vibrations. Measurements were continuously recorded, filtered to remove vibrations from the vehicle, and then used to estimate the coefficient values. In this case, the airspeed matches the vehicle speed that was limited to 150 km/h (36 m/s) for safety reasons.

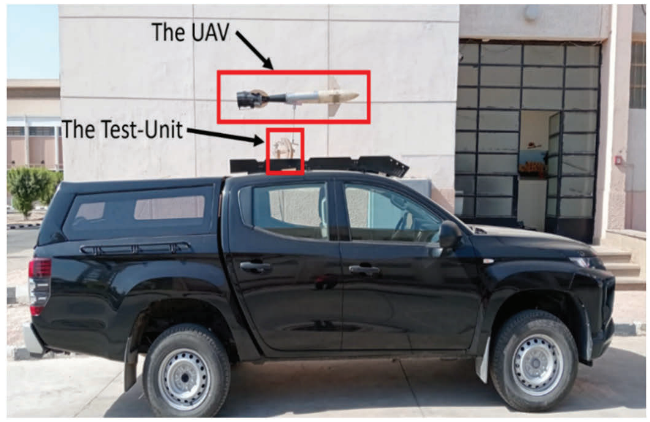

Fig. 27. The forces measurements using ground vehicle.

It is important to mention that the road chosen during the test was empty of potholes, cracks, and uneven surfaces to avoid vibration due to these issues.

Tables 6 and 7 show the values of the lift and drag coefficients using the previously used various approaches at two different AOA. The experiments are performed at a velocity of 10 m/s and the values are evaluated by comparing them with the ready-made wind tunnel as the trusting ratio of this measurement approach is higher than the other methods. So, to ensure consistency between these different approaches, we consider the results of real-wind experiments as the most reliable and accurate representation of the vehicle's aerodynamic behavior.

The real-wind experiments closely mimic the actual flight conditions and provide the most direct, real-world data for aerodynamic performance. Therefore, the results from the real-wind experiments serve as our primary reference and benchmark for validating all other aerodynamic modeling approaches. So the error percentages presented in Tables 6 and 7 refer to the error according to the wind-tunnel results, and the value of the relative error was presented.

Table 6. The lift coefficient estimation using various approaches.

AOA	Wind tunnel	DATCOME		CFD		Implemented wind tunnel		Using ground-vehicle	
	Value	Value	RE	Value	RE	Value	RE	Value	RE
5	0.491	0.346	29%	0.471	4.07%	0.48	2.2%	0.52	5.9%
10	0.981	0.717	26.91%	0.932	4.99%	0.95	3.1%	0.92	6.2%

Table 7. The drag coefficient estimation using various approaches.

AOA	Wind tunnel	DATCOME		CFD		Implemented wind tunnel		Using ground-vehicle	
	Value	Value	RE	Value	RE	Value	RE	Value	RE
5	0.201	0.144	28.35%	0.231	14.9%	0.221	9.95%	0.18	10.44%
10	0.31	0.23	25.80%	0.324	4.51%	0.321	3.54%	0.35	12.9%

4.5. *Propulsion system*

Modeling the propulsion system is crucial for creating a high-fidelity and reliable simulation environment for the overall UAV model. Therefore, developing an accurate and dependable model is a key focus in the UAV design [38]. In our case study, the propulsion system features an electric ducted fan (EDF) motor, which is regulated by an electronic speed controller (ESC). The ESC controls the speed of the motor by adjusting the current values. Our propulsion model is treated as a black box, with the throttle value as the input and the thrust force as the output.

The propulsion system used is the Mercury EDF, which is constructed from full alloy using high-precision CNC machining and provides excellent thermal dissipation. It includes an 11-blade rotor made of aluminum that supports high rotation speeds. The front "spinner" remains stationary to reduce vibration risk and is safeguarded by two sets of four stators to prevent rotor ejection. Additionally, the brushless motor is positioned at the front of the EDF to enhance heat dissipation. Table 8 shows the Mercury EDF parameters.

The process of system identification is used to estimate a mathematical model of the propulsion system, specifically the motor and its associated components, based on experimental data. The following paragraphs explain a detailed breakdown of the experimental setup, data collection process, system identification, model estimation, and validation as described in this experiment.

The system identification procedure begins with data collection through a carefully designed experimental setup. The main components of this setup are shown in Figs. 28 and 29 which include the following:

- Throttle Input Control: The throttle input is controlled remotely via a Remote Controller (RC), which is used to command the motor to operate at varying power levels. The RC sends control signals that are converted into a PWM signal by the Electronic Speed Controller (ESC). PWM is a standard method for controlling the speed of DC motors by modulating the duty cycle of the signal sent to the motor.
- Motor and Propeller: The PWM signal controls the speed of the EDF motor, which drives a propeller. The speed at

Table 8. The mercury EDF parameters.

Parameter	Value
Characteristics/LIPO	6 s
Voltage	22.2 v
Current	115 A
Power	2250 W
Thrust	5.2 kg constant — 5.8 kg max
Controller	>=130 A/LV
Recommended battery	>= 3000 mAh 35 C
Duct inside diameter	104 mm
Total weight	435 g
Blades number	11 (CNC aluminum)
Motor timing	Low or 2 degree

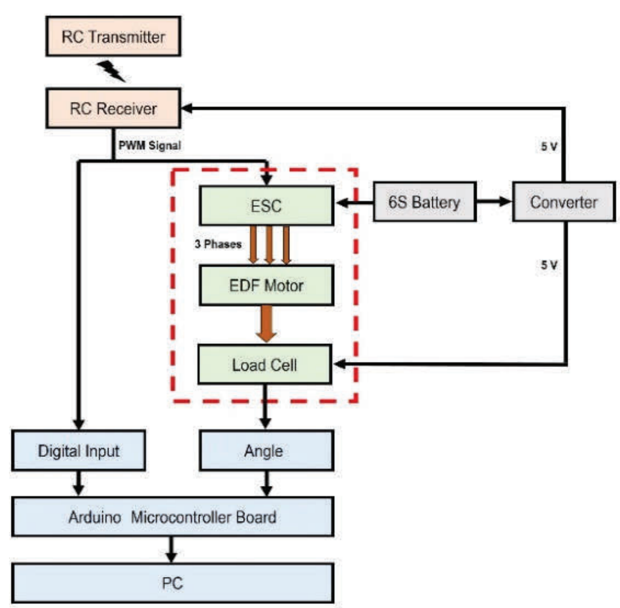

Fig. 28. Block diagram for the propulsion identification.

Fig. 29. The experimental setup of the propulsion system identification.

which the motor operates (in terms of Revolutions per Minute (RPM)) corresponds to the PWM input, which is controlled via the throttle setting.

- Load Cell for Thrust Measurement: The load cell is used to measure the thrust force generated by the motor and propeller. The load cell converts the physical force into an electrical signal. This signal is then sent to a microcontroller (Arduino) through an Analog-to-Digital Converter (ADC).
- Data Acquisition and Control: The setup also includes a microcontroller (Arduino) that manages the system. It receives data from the load cell and the PWM signal and sends them to MATLAB®/Simulink for system identification. The ESC is powered by a 6-cell battery, which provides the required current to drive the motor.
- Sampling Frequency: Data are collected at a frequency of 50 Hz, which means that every 20 ms, a new set of data (throttle input and corresponding thrust force) is recorded.
- Wireless Communication: The throttle input commands are transmitted wirelessly from a controller (probably a laptop or another remote device) to the Arduino.

Before collecting real motor data, the load cell needs to be calibrated. The calibration process involves using standard weights ranging from 1 kg to 2 kg. This ensures that the load cell is able to correctly measure thrust force and convert it into a corresponding digital value through the ADC. Calibration helps in ensuring that the measurement system is accurate and consistent.

After calibration, the load cell is connected to the Arduino, which will read the analog output and convert it to digital signals for further processing.

Once the system is calibrated, the motor is attached to the load cell, and the system begins collecting data. The throttle input is varied in a step-wise manner, and the corresponding thrust output is measured at each step. However, raw data often contain noise due to several factors:

- Wireless interference in the communication between the remote controller and the Arduino.
- Inherent noise in the load cell and the electronics involved in signal acquisition might introduce random fluctuations or errors in the thrust measurements.

The raw data for the input and output are shown in Fig. 30. As shown, they are noisy and unsuitable for direct use in system identification.

To ensure accurate system identification, noise filtering is essential. The raw input and output data undergo a filtering process to remove noise and obtain a cleaner dataset. The purpose of filtering is to smooth out the random fluctuations that could distort the system's true behavior and affect the accuracy of the model.

The filtered dataset shown in Fig. 31 accurately represents filtered data, the clean data are then used for system identification. With the filtered data, we move to the core of system identification, where the goal is to find a mathematical model that describes the relationship between the input (throttle) and the output (thrust force). Several types of models are considered in the identification process:

Linear Models:

- Transfer Functions: Linear transfer functions describe the relationship between input and output in the frequency domain.
- Linear Polynomials: These models represent the relationship between input and output using polynomial equations.

Nonlinear Models:

Nonlinear Autoregressive with Exogenous Input (NLARX): This is a nonlinear model that incorporates the current and past inputs (throttle) and past outputs (thrust) to predict future outputs. This is particularly useful for capturing more complex relationships between input and output, which cannot be captured by linear models.

Once the models are estimated, they have to be validated. Validation involves comparing the model's predictions to actual experimental data that were not used during the model identification phase. The validation data serve as a test set to evaluate how well the identified model generalizes to new, untested conditions.

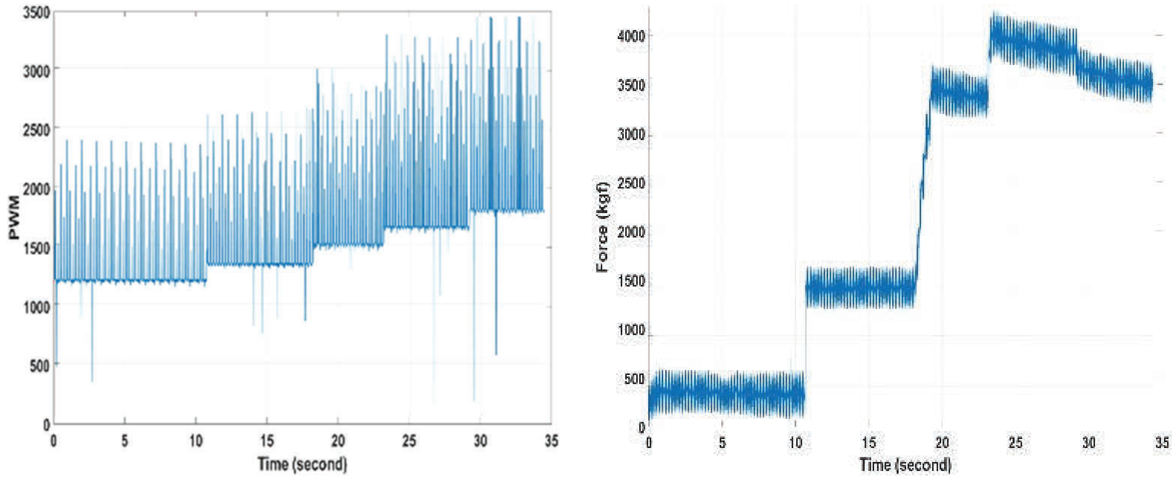

(a) *Input PWM*

(b) *Output Thrust*

Fig. 30. The raw input and output dataset.

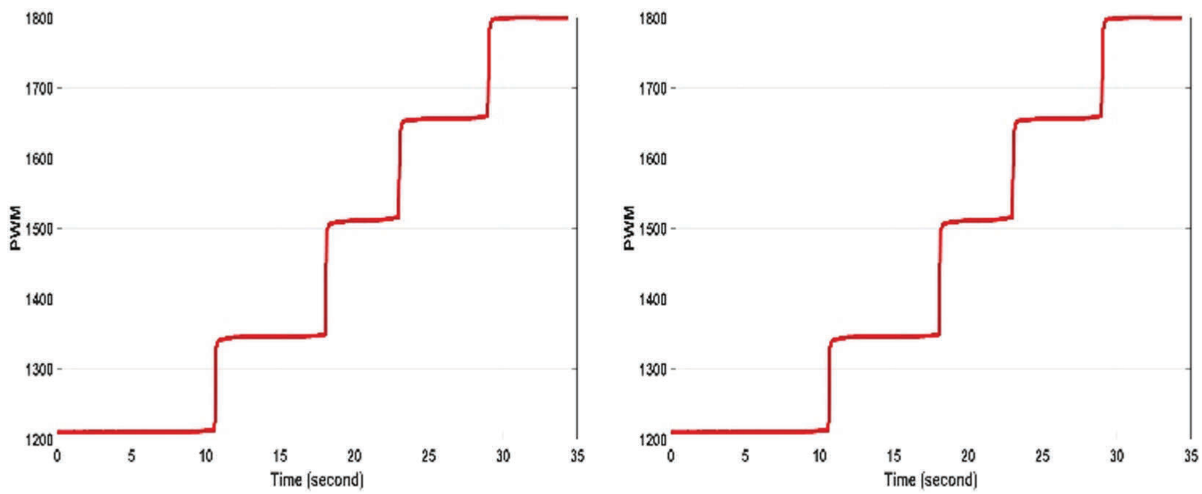

(a) *Input PWM*

(b) *Output Thrust*

Fig. 31. The filtered input and output dataset.

The validation process includes the following:

- Generating a Model-Based Estimate: The identified model (whether linear or nonlinear) is used to predict the thrust output for any given throttle input.
- Comparing Model Output to Measured Data: The predicted thrust is compared to the actual thrust measured by the load cell. If the predicted output is close to the measured output, the model is considered a good fit.
- Best Fit Selection: Different models (linear and nonlinear) are tested, and the one that provides the best match to the experimental data is selected as the optimal model.

In this case, the Nonlinear Autoregressive with Exogenous Input (NLARX) model is determined to be the best model for representing the propulsion system. This model is particularly suitable for systems that exhibit nonlinear behavior, such as electric propulsion motors, where the relationship between input (throttle) and output (thrust) can be highly complex.

Finally, the identified NLARX model is implemented in Simulink for simulation and further analysis. Simulink provides a platform for designing, simulating, and testing the propulsion system model. Using the estimated NLARX model, we can simulate the system's response to varying throttle inputs and predict the thrust output under different operating conditions (Fig. 32).

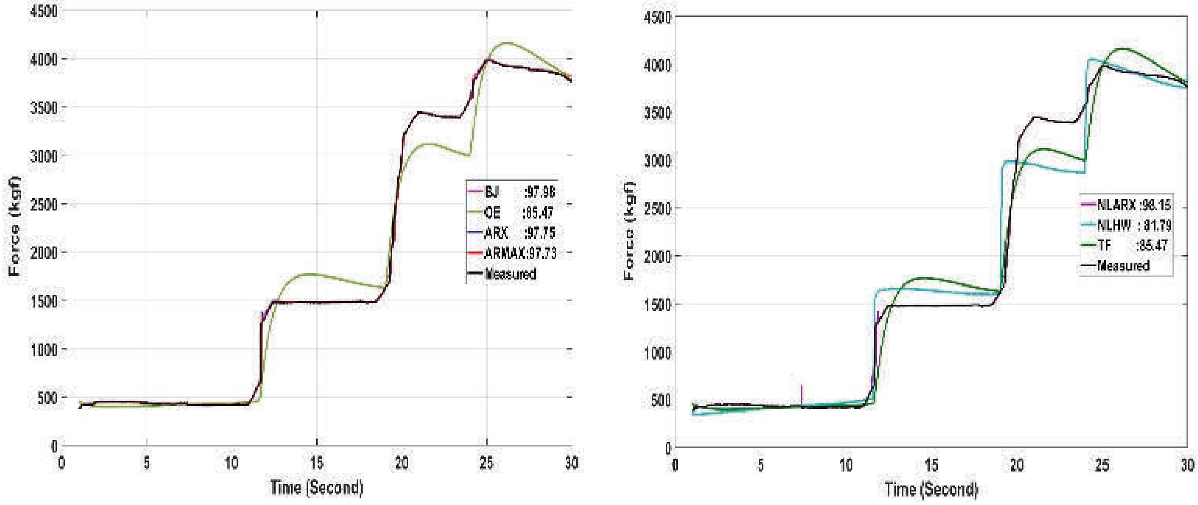

(a) (b)

Fig. 32. The propulsion system identification models.

4.6. *The trimming*

The trim operating point refers to the specific set of conditions under which an aircraft, UAV, or vehicle operates in a state of equilibrium or steady flight. At this point, all the forces and moments acting on the vehicle are balanced, and no further control inputs are needed to maintain a steady state.

There are two methods to calculate the trim data, one is the approximated analytical solution which requires a linearized aerodynamic model, and the other is the graphical solution.

The trimming process was calculated using an approximated analytical solution in Simulink with the Model Linearization Tool. A fixed step size of 0.01 was used, and the Euler solver was applied for numerical integration. This approach allowed for the calculation of the trim conditions, such as steady-state flight parameters, by solving the linearized system of equations that describe the vehicle's dynamics. The use of a fixed step size ensures that the simulation time steps are consistent, while the Euler solver provides a simple numerical method for solving the system's equations, enabling efficient trimming of the model.

4.7. *Open loop simulation results and analysis*

The UAV sub-models discussed earlier are combined to create a 6-DOF model in MATLAB® (Simulink), as illustrated in Fig. 33. This model needs to pass the verification and validation processes. Initially, verification is conducted by testing a flight maneuver to ensure the model produces

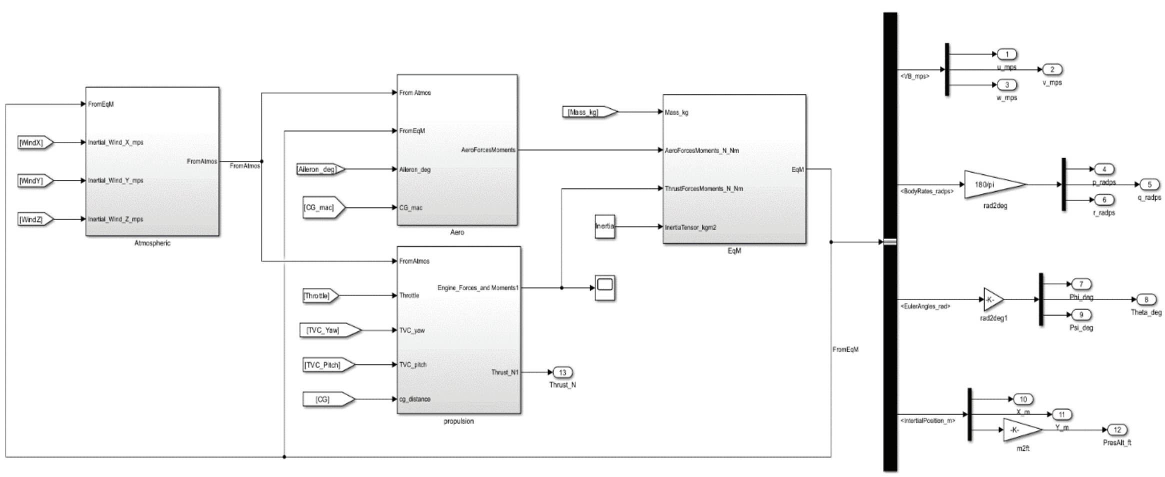

Fig. 33. The 6-DOF model using Simulink.

acceptable results, Validation will subsequently be carried out using a flight test for the UAV case study.

The longitudinal motion can be excited by deflecting the TVC unit in the vertical plane as shown in Fig. 34. The UAV pitch down-up maneuver agrees with the defection degrees positive-negative input, angle of attack, pitching rate variation, and pitch angle are cleared. It's clear that this motion is stable and has a rapid damped oscillation.

Figure 35 shows the Calibrated Airspeed (CAS) that refers to the speed of the UAV as measured by its airspeed indicator, corrected for instrument and position errors but not for changes in altitude or temperature. CAS is used in aviation to provide a more accurate measurement of airspeed than indicated airspeed (IAS) alone, particularly in varying flight conditions. This calibrated airspeed is crucial for flight planning, performance calculations, and safe operation of the UAV. As shown, the value of the CAS in the *x*-axis is stable and with initial disturbance due to the applied TCV deflection.

Figure 36 shows the altitude variation due to the TVC defection and the load factor estimation, the load factor refers to the ratio of the aerodynamic force (or load) acting

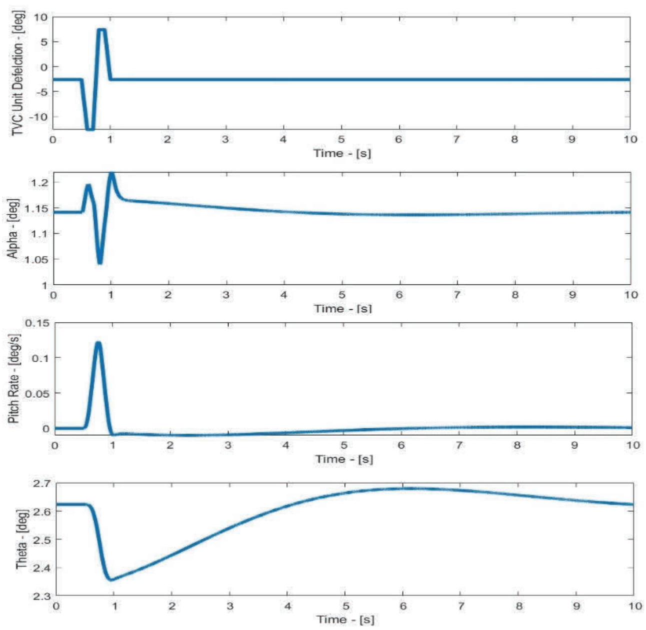

Fig. 34. The TVC deflection, AOA, pitch rate, and theta vs. time.

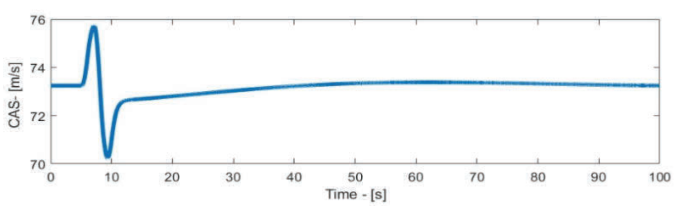

Fig. 35. The calibrated airspeed vs. time.

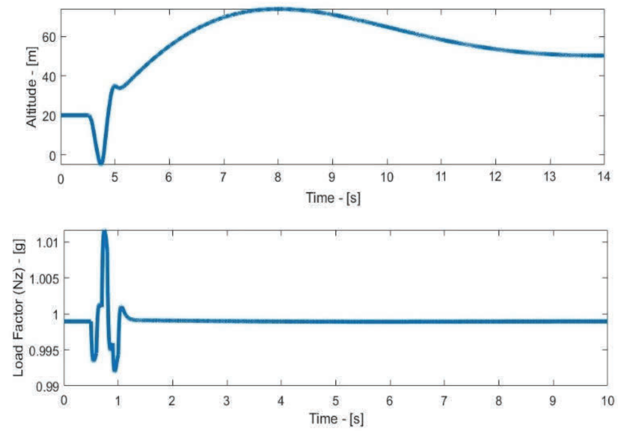

Fig. 36. The altitude variation and load factor vs. time.

on a body to the weight of the body. It is a measure of the amount of stress or load the aircraft is experiencing in relation to its own weight.

As shown, the body gains initial altitude due to the applied deflection that reaches a steady-state level after reaching the TVC deflection at its initial value. Because of the variation in the trust vector, the value of the load factor also will be varied during the applied deflection that reaches its stable value after finishing the deflection.

Wind with its stochastic nature has an effect on the body's flight parameters. This wind affects the relative velocity of the body with respect to surrounding air and hence affects the aerodynamic forces and moments acting on it. To generate a turbulence signal with the correct characteristics, a unit variance and a band-limited white noise signal are passed through or used in the appropriate filters. These filters are ultimately derived from the turbulence spectra. Three forms of filters are covered in the military references MIL-HDBK-1797 and MIL-F-8785C [40–42].

- Continuous Von Karman.
- Continuous Dryden.
- Discrete Dryden.

Components of wind using Continuous Dryden Spectrum are shown in Fig. 37.

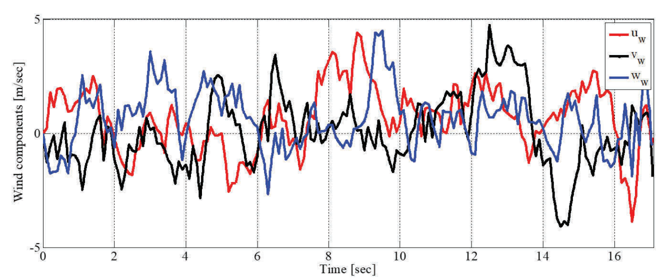

Fig. 37. The wind components.

Figures 38–40 show the results with disturbance.

It is clear from the behavior of the body that as the wind affects the body flight parameters, it remains stable and the mathematical model is valid for aerial vehicle simulation even in windy environment. The rubbles are insignificant and can be neglected.

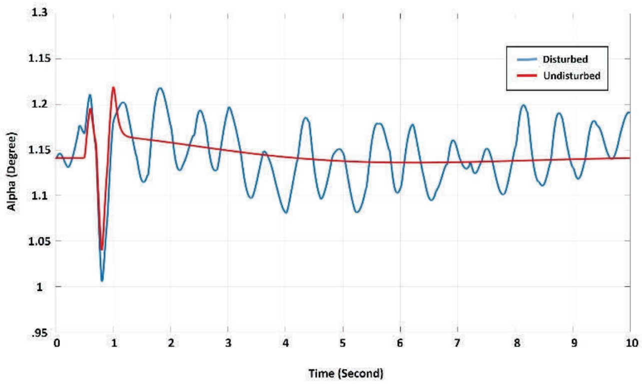

Fig. 38. The effect of wind on angle of attack.

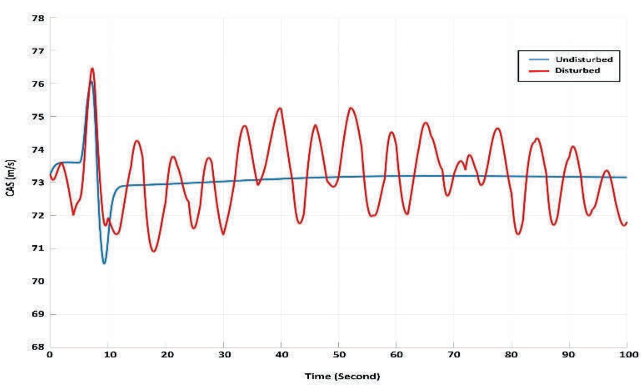

Fig. 39. The effect of wind on the calibrated airspeed.

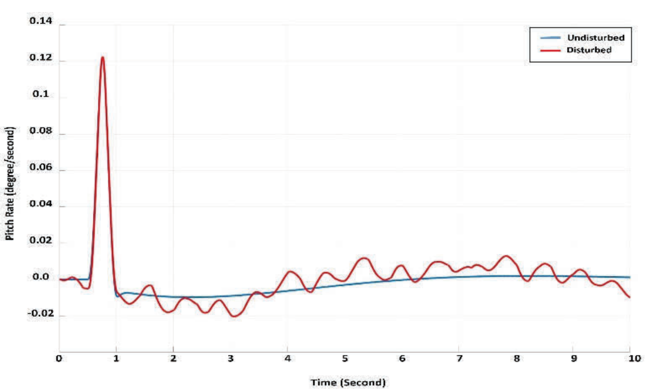

Fig. 40. The effect of wind on the pitch rate.

4.8. *Conclusion*

This work has developed a comprehensive six degrees-of-freedom (6DOF) simulation model for thrust vector control aerial vehicles (TVC-AVs), showcasing its accuracy and effectiveness in modeling, evaluating, and simulating the dynamic behavior of such vehicles. The approach involves breaking down the complex vehicle dynamics into five distinct sub-models, including aerodynamic characteristics estimated by using the semi-empirical techniques, computational fluid dynamics (CFD), and wind-tunnel experiments.

The validation of aerodynamic coefficients and derivatives, alongside low-cost wind-tunnel testing and experimental investigation of mass-inertia properties, contributes to a high-fidelity model. The atmospheric model is constructed using The International Standard Atmosphere (ISA) values, and the actuation model is validated through system identification.

Integration of these sub-models into a nonlinear dynamics framework within MATLAB® (Simulink) allows for precise trim value determination and model verification. The resulting open-loop simulation effectively captures the body motion and behavior of the TVC-AV, facilitating the design of robust flight controllers and guidance systems.

This study underscores the significance of combining experimental data with advanced simulation techniques to enhance the performance and maneuverability of aerial vehicles based on the TVC, particularly in conditions where classical aerodynamic controls are insufficient. The validated model serves as a valuable tool for future research and development in aerial vehicle control systems, ensuring more accurate predictions and improvements in dynamic aerobatics and stability, even at high angles-of-attack and near-zero airspeeds.

ORCID

Mohamed M. Ahmed https://orcid.org/0009-0003-9408-470X
Gamal M. ElBayoumi https://orcid.org/0009-0005-5029-3459
Ahmed E. Elbanna https://orcid.org/0009-0007-7589-7405

References

[1] W. D. Nutter, D. M. Wright and P. R. Stryker, Thrust vector control for enhanced performance of a small unmanned aerial vehicle, *J. Guid. Control Dyn.* **38**(1) (2015) 45–54.

[2] P. J. McCormick and H. W. Lee, Analysis and optimization of thrust vector control for high-performance rocket systems, *Aerosp. Sci. Technol.* **32**(3) (2014) 125–136.

[3] T. A. Lawrence, J. L. Roberts and S. M. Bell, Adaptive thrust vector control systems for advanced aerospace applications, *Control Eng. Pract.* **52** (2016) 104–116.

[4] R. J. Anderson and M. C. Wilson, Design and implementation of a thrust vector control system for reusable launch vehicles, *J. Aerosp. Eng.* **30**(4) (2017) 04016070.

[5] S. G. Simon and M. T. Lee, Comparative study of thrust vector control techniques for small satellite launch vehicles, *J. Propuls. Power* **31**(5) (2015) 1482–1493.

[6] D. A. Smith and E. J. Martin, Thrust vector control for high-angle-of-attack maneuvering in hypersonic vehicles, *AIAA J.* **55**(9) (2017) 2802–2811.

[7] L. P. Taylor and J. K. Cooper, Dynamic modeling and control of thrust vector actuators for precision launch vehicle guidance, *J. Aerosp. Inf. Syst.* **13**(11) (2016) 396–408.

[8] M. S. Edwards and K. S. Wong, Thrust vector control in advanced aerospace vehicles: An overview of recent developments, *J. Aerosp. Syst.* **21**(2) (2014) 67–84.

[9] F. J. Garcia and R. K. Patel, Thrust vector control algorithms for improving stability and control of high-speed aircraft, *J. Aircr.* **53**(4) (2016) 1005–1018.

[10] H. J. Robinson and J. A. Evans, Application of thrust vector control to small-scale space launch systems, *Space Sci. Rev.* **192**(1–4) (2015) 161–177.

[11] E. H. Kapeel, M. A. H. Abozied, A. M. Kamel and H. Hendy, Physical modeling, simulation and validation of small fixed-wing UAV, *Unmanned Syst.* **11**(04) (2022) 327–350.

[12] A. Harris Antony *et al.*, Thrust vector control in rockets: Methods and effects, *Int. J. Adv. Res. Ideas Innov. Technol.* **8**(4) (2022) 218–255.

[13] N. M. Jodeh, *Development of Autonomous Unmanned Aerial Vehicle Research Platform: Modeling, Simulating, and Flight Testing* (Air Force Institute of Technology, Wright-Patterson Air Force Base, Ohio, 2006).

[14] A. Ünal, Design and implementation of a thrust vector control (TVC) test system, *J. Polytech.* **21**(2) (2018) 497–505.

[15] P. dos Santos, Thrust vector control and state estimation architecture for low-cost small-scale launchers, *Electr. Eng. Syst. Sci.* ArXiv abs/2303.16983 (2023).

[16] L. Sopegno *et al.*, Thrust vector controller comparison for a finless rocket, *Machines* **11**(3) (2023) 394.

[17] E. R. Mueller, Hardware-in-the-loop simulation design for evaluation of unmanned aerial vehicle control systems, *AIAA SciTech Forum* (2007).

[18] H. In and E. Leong, Development of a 6DOF nonlinear simulation model enhanced with fine tuning procedures, in *Proc. Conf.* (2008).

[19] G. Skorobogatov, C. Barrado and E. Salamí, Multiple UAV systems: A survey, *J. Unmanned Syst.* **8**(2) (2020) 149–169.

[20] G. Cai, J. Dias and L. Seneviratne, A survey of small-scale unmanned aerial vehicles: Recent advances and future development trends, *J. Unmanned Syst.* **2**(2) (2014) 175–199.

[21] K. S. Kumar and A. M. Rasheed, Development of rotary wing mini UAS for civilian applications, *J. Unmanned Syst.* **1**(2) (2013) 247–258.

[22] S. H. Derrouaoui, Y. Bouzid, M. Guiatni and I. Dib, A comprehensive review on reconfigurable drones: Classification, characteristics, design and control technologies, *J. Unmanned Syst.* **10**(1) (2021) 3–29.

[23] Y. Ding, B. Xin and J. Chen, A review of recent advances in coordination between unmanned aerial and ground vehicles, *J. Unmanned Syst.* **9**(2) (2021) 97–117.

[24] C. Zammit and E.-J. van Kampen, Real-time 3D UAV path planning in dynamic environments with uncertainty, *J. Unmanned Syst.* **11** (2023) 203–219.

[25] R. Yanushevsky, *Guidance of Unmanned Aerial Vehicles*, 1st edn. (CRC Press, Boca Raton, 2011).

[26] E. Safwat, M. A. H. Abozied, A. M. Kamel and Y. Z. Elhalwagy, Path following design and analysis for small UAV based on adaptive modified incremental backstepping, *AIAA Science and Technology Forum and Exposition, AIAA SciTech Forum* (2022).

[27] E. Safwat, W. Zhang, A. Mohsen and M. Kassem, Design and analysis of a robust UAV flight guidance and control system based on a modified nonlinear dynamic inversion, *J. Appl. Sci.* **9**(17) (2019) 3600.

[28] E. Safwat and A. Kamel, Generic UAV autopilot prototype based on adaptive modified incremental backstepping, *AIAA SciTech Forum* (2021).

[29] K. M. Hafez, M. L. Shapiro and L. R. Edwards, A review of computational fluid dynamics (CFD) techniques for aerospace applications, *Aerosp. Sci. Technol.* **64** (2017) 76–98.

[30] S. T. Lee and D. M. Rowe, Enhanced CFD modeling techniques for turbulent flow simulations in aircraft design, *J. Fluid Mech.* **800** (2016) 1–24.

[31] R. J. Smith and A. L. Wilson, Applications of CFD in the optimization of aerodynamic performance for small unmanned aerial vehicles, *Comput. Fluids* **111** (2015) 13–28.

[32] L. W. Zhang, Y. M. Chen and J. T. Hong, Advanced CFD methods for predicting the flow field of hypersonic vehicles, *J. Aerosp. Eng.* **29**(3) (2016) 04016012.

[33] E. J. Morgan and H. F. Parker, Comparative study of CFD techniques for predicting aircraft wing performance, *J. Aircr.* **51**(2) (2014) 401–412.

[34] C. D. Johnson and K. P. Smith, CFD-based design and analysis of high-performance propellers for UAVs, *J. Propuls. Power* **31**(1) (2015) 175–186.

[35] R. W. Beard and T. W. Mclain, *Navigation, Guidance, and Control of Small and Miniature Air Vehicles*, 1st edn. (Princeton University Press, 2012).

[36] E. Safwat, W. Zhang, Y. Lyu and M. Kassem, Nonlinear dynamic inversion flight controller for small unmanned aircraft vehicle, in *2018 IEEE CSAA Guidance, Navigation and Control Conference (CGNCC)*, (IEEE, 2018), pp. 1–7.

[37] A. M. Kamal, A. M. Bayoumy and A. M. Elshabka, Modeling, analysis and validation of a small airplane flight dynamics, *AIAA Modeling and Simulation Technologies Conference* (AIAA, 2015).

[38] S. F. Shelan, M. A. Hassan, H. Hendy and Y. Z. Elhalwagy, FPGA-based controller for electro-mechanical fin actuation system using processor in the loop (PIL), *2020 12th International Conference on Electrical Engineering (ICEENG)*, (IEEE, 2020), pp. 363–370.

[39] E. H. Kapeel, M. A. H. Abozied, A. M. Kamel and H. Hendy, Evaluation of missile terminal guidance using software in loop (SIL), *2020 12th International Conference on Electrical Engineering (ICEENG)*, (IEEE, 2020), pp. 389–395.

[40] U.S. Military Handbook MIL-HDBK-1797, 19 December 1997.

[41] U.S. Military Specification MIL-F-8785C, 5 November 1980.

[42] S. Gage, Creating a unified graphical wind turbulence model from multiple specifications, *AIAA Modeling and Simulation Technologies Conference and Exhibit* (AIAA, 2003).

Mohamed M. Ahmed holds a Bachelor's degree in Electrical Engineering from the Military Technical College in Egypt and is currently working on his Master's degree in Control systems for UAVs. His academic and professional focus on the flight mechanics and control. He has high FPGA and MATLAB expertise, along with accepted experience in system analysis and design through simulation and modeling tools.

Gamal M. ElBayoumi is an Emeritus Professor at the aerospace engineering department, Cairo university in Egypt with a Ph.D. in digital control from the Cairo university in Egypt. He has been teaching at the college since 1979 and served as the head of the aerospace engineering department, overseeing research projects on unmanned systems. Dr. Gamal is an expert in the field of unmanned systems and His research interests include UAVs Guidance, Satellites, Inertial Navigation, and Autopilot Design. Dr. Gamal is widely recognized for his expertise and actively contributes to teaching and research in the Department of Aerospace Engineering at the Cairo University.

Ahmed E. Elbanna is a Lecturer at the Arab Academy for Science, Technology & Maritime Transport in Egypt. He earned his M.S. and Ph.D. degrees in Flight Guidance and Control from Benha University in 2010 and 2016, respectively. He completed his postdoctoral research at the National University of Defense Technology, China in 2023. Dr. Elbanna has published over 40 technical papers, with a primary research focus on UAV autopilot design. Since 2020, he has held the position of Vice Manager at the Unmanned Systems Guidance and Control Research Center, where he oversees research initiatives in UAV technology and contributes to advancements in unmanned systems development.